(d) Cross-link density, *XLD*

$$XLD = M_0/\bar{M}C \qquad M_0 = 14\ (polyethylene) \tag{4}$$

The mechanical properties of CLPE and CLPE-*g*-MPC with irradiation for 90 min were evaluated with tensile, impact, and creep deformation tests, as well as a shore hardness D measurement. Tensile testing was performed according to ASTM standard D638 using a type 4 tensile bar specimen and a crosshead speed of 50 mm/min. A double-notched (notch depth = 4.57 ± 0.08 mm) Izod impact strength test was performed to ASTM standard F648. Ten specimens were used in each tests. Creep deformation was measured by applying a constant load (113 kgf for 24 h) to a specimen, then measuring the height displacement, according to the ASTM D621 test method. Shore hardness D was measured according to the ASTM D2240 test method.

For all the test groups, the results derived from each experiment were expressed as mean values and the standard deviation. The statistical significance ($p < 0.05$) was judged by the Student's *t*-test.

TEM observation of cross section of CLPE-*g*-MPC

A cross section of the MPC polymer layer on the CLPE-*g*-MPC (90 min irradiation) surface before and after the hip joint simulator test was observed with a transmission electron microscope (TEM). Prior to observation, specimens were embedded in epoxy resin, stained in ruthenium oxide vapor at room temperature, and sliced into ultra-thin films. The specimen after the hip joint simulator test was coated with gold by sputter coater (JFC 1500, JEOL, Ltd., Tokyo, Japan) before embedding in resin. A JEM-1010 (JEOL, Ltd., Tokyo, Japan) was used for the TEM observation at an acceleration voltage of 100 kV.

Hip joint simulator test

The CLPE-*g*-MPC cups (26 mm inner diameter and 52 mm outer diameter) for testing in the hip joint simulator were gamma-ray sterilized under N_2 gas.

Friction torque between the CLPE-*g*-MPC cup and a 26 mm Co–Cr–Mo alloy femoral head (Japan Medical Materials Corp., Japan) was measured using a 2-station hip joint simulator (Kobe Steel, Ltd., Kobe, Japan). Measurements were performed with distilled water as lubricant, a loading of 280 kgf and a swing distance of 80 mm with a period of 1 Hz.

The in vitro wear test was performed using a 12-station hip joint simulator (MTS system Corp., MN, USA). A mixture of 25% bovine serum, 20 mM/L of ethylene diamine tetraacetic acid (EDTA), and 0.1% sodium azide was used as lubricant, according to the ISO 14242-1 standard. A load simulating a physiologic loading curve with double peaks of 183 and 280 kgf load was added with a period of 1 Hz. The wear was measured by a gravimetric method. The cup weights were measured every 0.5×10^6 cycles. The acetabular component was tested with a 26 mm Co–Cr–Mo alloy femoral head (Japan Medical Materials Corp., Japan). Testing then continued until a total of 3.0×10^6 cycles were completed.

Results

Figure 1 shows the FT-IR/ATR spectra of CLPE and CLPE-*g*-MPC. A transmission absorption peak was observed at 1460 cm^{-1} for both CLPE and CLPE-*g*-MPC. This peak is attributed mainly to the methylene chain in the CLPE substrate and MPC graft polymer. However, transmission absorptions at 1240, 1080 and 970 cm^{-1} were observed only for the CLPE-*g*-MPC. These peaks are due to the phosphate group in the MPC unit. Similarly, the transmission absorption at 1720 cm^{-1} observed for CLPE-*g*-MPC can only correspond to the carbonyl in the MPC unit.

Figure 2 shows the XPS spectra (N_{1s} and P_{2p}) of CLPE and CLPE-*g*-MPC. In the N_{1s} and P_{2p} spectra, clear peaks were observed only for CLPE-*g*-MPC. Peaks at 403 and 134 eV were assigned to the $-N^+(CH_3)_3$ and phosphate groups, respectively. These peaks were characteristic of the phosphorylcholine in the MPC unit. Table 1 summarizes the elemental composition of the untreated CLPE and the CLPE-*g*-MPC surfaces with various ultraviolet-ray irradiation times during polymerization. The content of nitrogen and phosphorous in the CLPE-*g*-MPC surface was increased to 5.1 and 5.2, respectively, with polymerization time. The elemental composition of the CLPE-*g*-MPC surface with a polymerization time of 90 min was almost

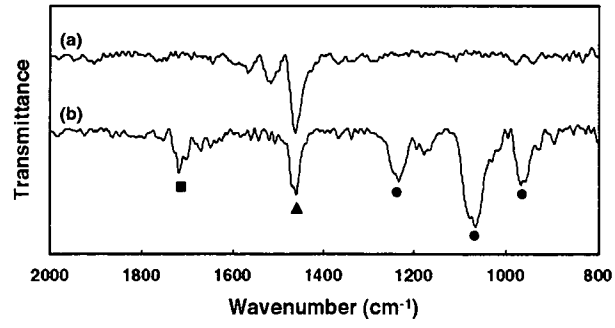

Fig. 1 FT-IR/ATR spectra of CLPE-*g*-MPC. (a) CLPE (untreated), (b) CLPE-*g*-MPC. •: P–O, ▲: CH_2, ■: C=O

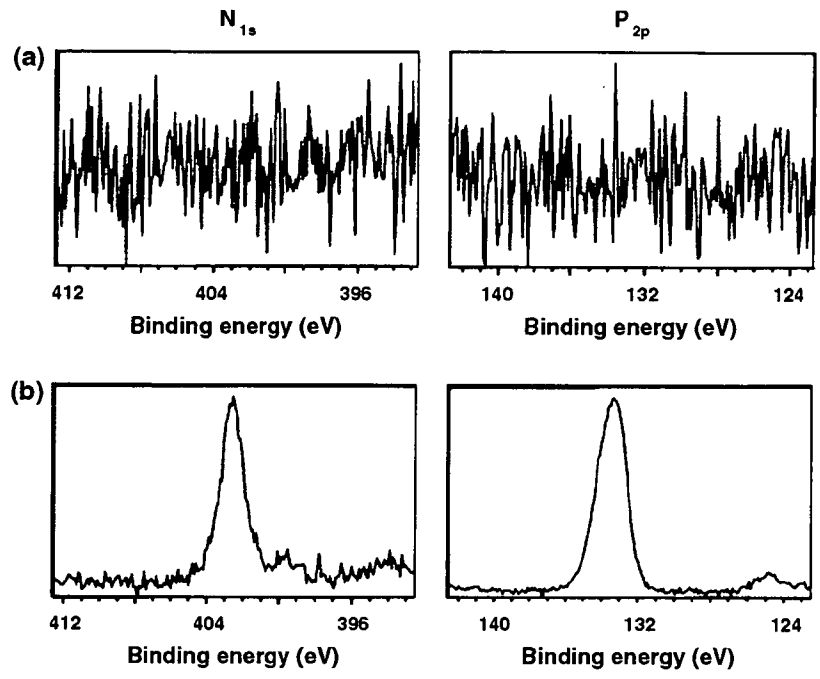

Fig. 2 XPS spectra of CLPE-*g*-MPC. (a) CLPE (untreated), (b) CLPE-*g*-MPC

Table 1 Surface elemental composition (%) of CLPE-*g*-MPC with various photo-polymerization times

Polymerization time (min)	C	O	N	P
0 (untreated CLPE)	99.6	0.4	0.0	0.0
12	96.6	3.4	0.0	0.0
23	78.5	17.0	1.9	2.7
45	60.4	30.2	4.1	5.3
90	61.8	27.9	5.1	5.2
MPC polymer*	57.9	31.6	5.3	5.3

*: Theoretical elemental composition of MPC polymer

equivalent to the theoretical elemental composition (N = 5.3, P = 5.3) of MPC polymer.

Figure 3 shows optical microscope images of moistened CLPE-*g*-MPC surfaces that were produced by various photo-irradiation times during polymerization. The surface image progressively alters from a hydrophobic surface to a hydrophilic one as polymerization time increases. On an untreated CLPE surface after spraying with water mist, typical hydrophobic behavior was observed, including the formation of many water droplets (Fig. 3a). In contrast, on the CLPE-*g*-MPC surface hydrophilic behavior was observed, characterized by a thin film of water (Fig. 3c).

The physical properties of CLPE and CLPE-*g*-MPC including density and swelling ratio are summarized in Table 2. It is generally said that energy irradiation to polyethylene causes a decrease in the swelling ratio. However, all of the bulk physical properties of CLPE and CLPE-*g*-MPC that were examined in this study differed little ($p < 0.05$) between the two materials.

The tensile yield strength, impact strength, creep deformation and shore hardness D of CLPE and CLPE-*g*-MPC are shown in Table 3. Tensile yield strength, impact strength and shore hardness D did not differ significantly ($p \leq 0.05$) between CLPE and CLPE-*g*-MPC, and both CLPE and CLPE-*g*-MPC met ASTM requirements (F648).

Figure 4 shows a TEM image of a cross section of CLPE-*g*-MPC. A grafted MPC polymer layer about 100 nm thick was observed on the CLPE substrate (Fig. 4b). Lamellae on the order of 100–400 nm long and 10–20 nm thick were observed in the CLPE substrate regardless of irradiation, and the lamellae were especially thin near the surface.

Table 4 shows the friction coefficient and the wear rate of the MPC polymer grafted CLPE cup in the hip joint simulator test. The friction coefficients of the untreated CLPE cups and the CLPE-*g*-MPC cups were 0.0075 and 0.0009, respectively. The CLPE-*g*-MPC cups reduced 88% in the friction coefficient compared with untreated CLPE cups, showed a high lubricity. We calculated the wear rate between 2.5×10^6 and 3.0×10^6 cycles. The wear rate of CLPE cups showed 3.12 mg/10^6 cycles. In contrast, the CLPE-*g*-MPC cups showed the reduction in wear to an essentially zero of −1.43 mg/10^6 cycles. The volumetric change was then calculated from the weight loss over time. In this study, the weight loss was calculated without considering the effect of water absorption.

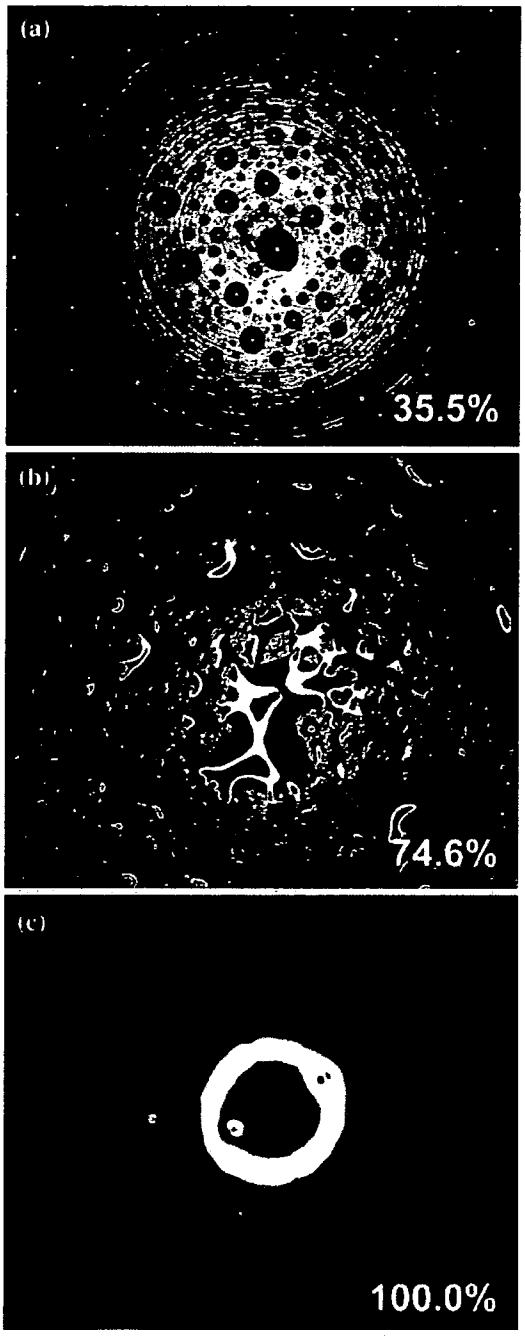

Fig. 3 Optical microscope images of CLPE-*g*-MPC cup surface with various photo-polymerization times. (**a**) 0 min (untreated CLPE), (**b**) 23 min and (**c**) 90 min. The water-covered ratio (%) is also shown. The white ring in (**c**) is due to the reflection of the light used in photography

Discussion

We have developed an artificial hip joint that uses CLPE-*g*-MPC on the bearing surface, with the goal of reducing wear and avoiding bone resorption. In this study, we investigated the effects of photo-induced radical graft polymerization technique on properties of the CLPE-*g*-MPC, and this report discusses the characteristics of the MPC polymer layer and the properties of the CLPE substrate.

After 3.0×10^6 cycles of the hip joint simulator test, we confirmed that the CLPE-*g*-MPC cups showed a quite low wear rate compared with untreated CLPE. Since MPC is a highly hydrophilic compound, and poly(MPC) is water-soluble, the water-wettability of the CLPE-*g*-MPC surface was greater than that of a CLPE surface due to the poly(MPC) chains, as shown in Fig. 3. It was observed that the CLPE-*g*-MPC surface supported a thin film of water. Consequently, the artificial hip joint bearing with an CLPE-*g*-MPC surface had high lubricity. The reduction in friction is assumed to have contributed to the improvement of anti-wear properties that was observed [22]. However, different processes such as migration of low molecular weight compounds, rotation of flexible polymer chains, inter- and intra-molecular rearrangements, and adhesion of contaminant particles, may take place at different rates depending on materials and ambient conditions [23]. Various factors such as type of bearing material, surface roughness, homogeneity of the surface and chemical composition affect the lubricity of the artificial joint [24]. In CLPE-*g*-MPC, the lubricity can change depending on the ambient conditions in vitro and in vivo. The bearing surface of the artificial hip joint with MPC polymer is assumed to have a structure similar to an artificial cell membrane, meaning this new concept artificial hip joint mimics the natural joint cartilage in vivo. To ensure the long-term retention of the benefits of this MPC polymer, we used photo-induced radical graft polymerization technique, to produce C–C covalent bonding between a carbon atom of the CLPE and the end-group of an MPC polymer chain. The results clearly show that the crystalline structure, physical and mechanical properties of the CLPE substrate were minimally changed, if at all, even after MPC grafting [25]. This indicates that photo-induced radical graft polymerization does not affect the properties of the CLPE substrate [18]. Retaining the properties of the CLPE substrate unchanged is very important in clinical use, because the CLPE cup acts not only as a bearing material but also as a structural material in the artificial hip joint system. Generally, increased cross-linking in the CLPE degrades its mechanical properties, producing a trade-off between wear-resistance and mechanical properties [5, 26]. It is desirable to reduce wear while maintaining the mechanical properties necessary for proper in vivo function. The advantage of photo-induced radical graft polymerization comes from the fact that the grafted MPC polymer gave a high lubricity only on the surface, and had no effect on the bulk properties of the CLPE substrate.

Table 2 Physical properties of CLPE-*g*-MPC

Sample	Density (g/cm^3)	Swelling ratio	Network chain density ($\times 10^3$ mol/ml)	M.W. between Cross-links (g/mol)	Cross-link density (mol%)
CLPE	0.944 (0.002)	2.99 (0.11)	0.437 (0.043)	2165 (214)	0.65 (0.06)
CLPE-*g*-MPC	0.943 (0.001)	2.94 (0.10)	0.459 (0.044)	2069 (186)	0.68 (0.07)

The standard deviation is in parentheses

Table 3 Mechanical properties of CLPE-*g*-MPC

Sample	Yield strength (MPa)	Impact strength (kJ/m^2)	Creep deformation (%)	Hardness (shore D)
CLPE	23.2 (0.4)	75.0 (1.4)	0.89 (0.17)	68.2 (0.9)
CLPE-*g*-MPC	23.1 (0.5)	77.0 (1.9)	0.63 (0.40)	68.4 (0.5)

The standard deviation is in parentheses

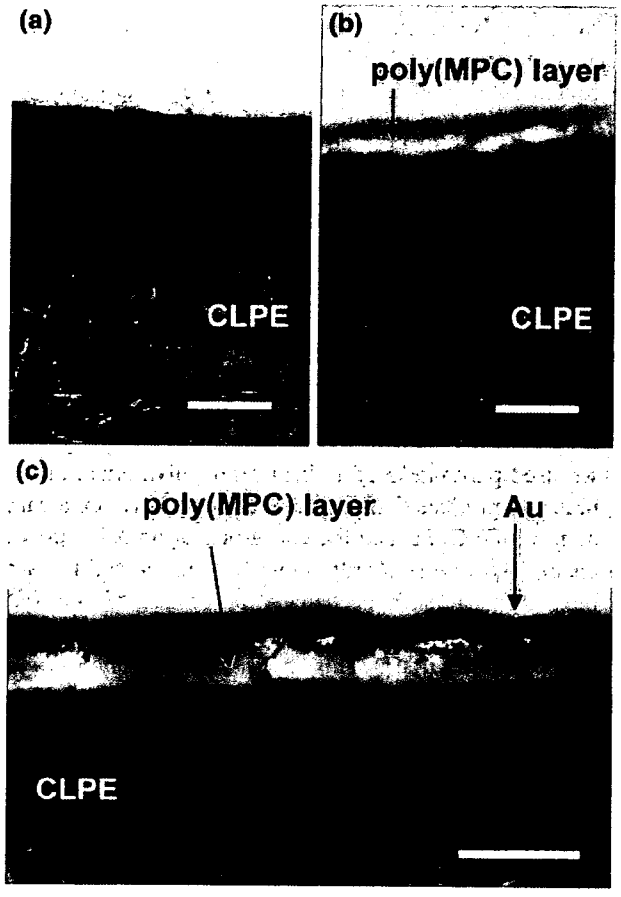

Fig. 4 Cross-sectional TEM images of CLPE-*g*-MPC. (**a**) CLPE (untreated), (**b**) CLPE-*g*-MPC before simulator test and (**c**) CLPE-*g*-MPC after a 3×10^6 cycle simulator test. Bar; 200 nm

After 3.0×10^6 cycles in the hip joint simulator test, the wear rate of CLPE-*g*-MPC cups remained low. The cross-sectional TEM image of the CLPE-*g*-MPC bearing surface after 3.0×10^6 cycles of the hip simulator test (Fig. 4c)

Table 4 Tribological properties of CLPE-*g*-MPC

Sample	Friction coefficient	Wear rate ($mg/10^6$ cycles)
CLPE	0.0075	3.12
CLPE-*g*-MPC	0.0009	−1.43

showed that most of the bearing surface was covered by the MPC polymer layer even after the hip simulator test. In other words, the CLPE-*g*-MPC cups showed little wear on inspection, supporting the quite low wear observed in the hip joint simulator test.

On the CLPE-*g*-MPC surface, the nitrogen and phosphorus attributed to the phosphorylcholine in the MPC units increased with increasing polymerization time. This indicates that the density of the grafted MPC polymer can be controlled by the polymerization time, since the number of polymer chains produced in a radical polymerization is generally proportional to the photo-irradiation time. The elemental composition obtained by XPS (N = 5.1, P = 5.2) of the CLPE-*g*-MPC surface with a polymerization time of 90 min was almost equivalent to the theoretical elemental composition of MPC polymer. Therefore, the entire surface of the CLPE was assumed to be coated with an MPC polymer layer.

However, the area observed by the X-ray spot (approximately 400×800 μm^2) in XPS was quite limited. As a supplementary probe to examine the MPC polymer layer, wettability measurement of cups should be performed on many separate areas on the cups. The wettability measurement of a surface is readily performed in the laboratory on well defined, homogeneous, smooth and planar surfaces of prepared specimens. In the case of artificial hip joint cups, for which non-destructive measurements are usually required (and where excision of material samples is usually undesirable), these conditions do not exist and measurement with high precision is a difficult task. Hence,

we evaluated wettability of CLPE-*g*-MPC cup by the spray method, because this method can be used non-destructively on large areas.

Since CLPE-*g*-MPC reduces the production of wear particles and bone-resorptive responses, periprosthetic osteolysis could be eliminated [12]. Based on the mechanical, tribological and biological advantages, we confidently expect CLPE-*g*-MPC be used in the next-generation of artificial hip joint systems.

Conclusions

In this study, effects of a photo-induced radical graft polymerization technique on physical, mechanical and tribological properties of CLPE-*g*-MPC were investigated. The crystalline structure, physical and mechanical properties of the CLPE substrate were unchanged after the addition of a layer of MPC polymer by photo-polymerization. However, CLPE-*g*-MPC cups reduced 88% in the friction coefficient compared with untreated CLPE cups. After 3.0×10^6 cycles in the hip joint simulator test, the wear rate of CLPE-*g*-MPC cups remained low. We concluded that the advantage of this photo-induced radical graft polymerization technique was that the grafted MPC polymer layer produces high lubricity while only affecting the surface, and has no effect on the properties of the CLPE substrate.

Acknowledgements This work was supported by a Grant-in-Aid for Scientific Research from the Japanese Ministry of Education, Culture, Sports, Science and Technology (#15390449), and a Health and Welfare Research Grant for Translational Research from the Japanese Ministry of Health, Labour and Welfare. The authors also express special thank to Dr. Fumiaki Miyaji, Mr. Yoshiki Ando and Mr. Takatoshi Miyashita (Japan Medical Materials Corp., Japan) for their excellent technical assistance.

References

1. W. H. HARRIS, *Clin. Orthop.* **311** (1995) 46
2. A. KOBAYASHI, M. A. FREEMAN, W. BINEFIELD, Y. KADOYA, T. YAMAC, N. AL-SAFFER, G. SCOTT and P. A. REVELL, *J. Bone Joint Surg.* **79**(5) (1997) 844
3. D. H. SOCHART, *Clin. Orthop.* **363** (1999) 135
4. O. K. MURATOGLU, A. MARK, D. A. VITTETOE, W. H. HARRIS and H. E. RUBASH, *J. Bone Joint Surg.* **85A** (2003) 7
5. H. MCKELLOP, F. W. SHEN, B. LU, P. CAMPBELL and R. SALOVEY, *J. Orthop. Res.* **17**(2) (1999) 157
6. O. K. MURATOGLU, C. R. BRAGDON, D. O. O'CONNOR, M. JASTY and W. H. HARRIS, J. Arthroplasty 16 (2001) 149
7. D. W. MANNING, P. P. CHIANG, J. M. MARTELL, J. O. GALANTE and W. H. HARRIS, *Orthop. Res. Soc.* (2004) 1478
8. G. DIGAS, J. KÄRRHOLM, J. THANNER, H. MALCHAU and P. HERBERTS, *Clin. Orthop. Relat. Res.* **417** (2003) 126
9. C. HEICEL, M. SILVA, M. A. DELA ROSA and T. P. SCHMALZRIED, *J. Bone Joint Surg. Am.* **86**(4) (2004) 748
10. J. M. MARTELL, J. J. VERNER and S. J. INCAVO, *J. Arthroplasty* **18**(7) (2003) 55
11. H. OONISHI, S. C. KIM, Y. TAKAO, M. KYOMOTO, M. IWAMOTO and M. UENO, *J. Arthroplasty* **21**(7) (2006) 944
12. T. MORO, Y. TAKATORI, K. ISHIHARA, T. KONNO, Y. TAKIGAWA, T. MATSUSHITA, U. I. CHUNG, K. NAKAMURA and H. KAWAGUCHI, *Nature Mater.* **3** (2004) 829
13. K. ISHIHARA, R. ARAGAKI, T. UEDA, A. WATANABE and N. NAKABAYASHI, *J. Biomed. Mater. Res.* **24** (1990) 1069
14. K. ISHIHARA, N. P. ZIATS, B. P. TIERNEY, N. NAKABAYASHI and J. M. ANDERSON, *J. Biomed. Mater. Res.* **25**(11) (1991) 1397
15. K. J. KUIPER and J. E. NORDREHAUG, *Am. J. Cardiol.* **85** (2000) 698
16. M. GALLI, L. SOMMARIVA, F. PRATI, S. ZERBONI, A. POLITI, R. BONATTU, S. MAMELI, E. BUTTI, A. PAGANO and G. FERRARI, *Cathet. Cardiovasc. Intervent.* **53** (2001) 182
17. A. L. LEWIS, L. A. TOLHURST and P. W. STRATFORD, *Biomaterials* **23** (2002) 1697
18. K. ISHIHARA, Y. IWASAKI, S. EBIHARA, Y. SHINDO and N. NAKABAYASHI, *Colloids Surf. B, Biointerfaces* **18** (2000) 325
19. K. ISHIHARA, T. UEDA and N. NAKABAYASHI, *Polym. J.* **22**(5) (1990) 355
20. Swedish Transmission Research Institute, "Hydrophobicity Classification Guide", Guide 1, 92/1 (1992)
21. F. W. SHEN, H. A. MCKELLOP and R. SALOVEY, *J. Polym. Sci. Part B, Polym. Phys.* **34** (1996) 1063
22. M. H. NAKA, Y. MORITA and K. IKEUCHI, *Proc. Inst. Mech. Eng. [H]* **219**(3) (2005) 175
23. U. RAVIV, J. FREY, R. SAK, P. LAURAT, R. TADMOR and J. KLEIN, *Langmuir* **18** (2002) 7482
24. S. P. HO, N. NAKABAYASHI, Y. IWASAKI, T. BOLAND and M. LABERGE, *Biomaterials* **24** (2003) 5121
25. K. ISHIHARA, D. NISHIUCHI, J. WATANABE and Y. IWASAKI, *Biomaterials* **25** (2004) 1115
26. O. K. MURATOGLU, C. R. BRAGDON, D. O. O'CONNOR, M. JASTY, W. H. HARRIS, R. GUL and F. MCGARRY, *Biomaterials* **20** (1999) 1463

OPEN ACCESS Freely available online

PLoS one

GSK-3β Controls Osteogenesis through Regulating Runx2 Activity

Fumitaka Kugimiya[1,2], Hiroshi Kawaguchi[2], Shinsuke Ohba[1], Naohiro Kawamura[2], Makoto Hirata[2], Hirotaka Chikuda[2], Yoshiaki Azuma[3], James R. Woodgett[4], Kozo Nakamura[2], Ung-il Chung[1]*

1 Center for Disease Biology and Integrative Medicine, University of Tokyo, Tokyo, Japan, 2 Sensory and Motor System Medicine, Faculty of Medicine, University of Tokyo, Tokyo, Japan, 3 Teijin Institute for Biomedical Research, Tokyo, Japan, 4 Ontario Cancer Institute, Princess Margaret Hospital, Toronto, Canada

Despite accumulated knowledge of various signalings regulating bone formation, the molecular network has not been clarified sufficiently to lead to clinical application. Here we show that heterozygous glycogen synthase kinase-3β (GSK-3β)-deficient mice displayed an increased bone formation due to an enhanced transcriptional activity of Runx2 by suppressing the inhibitory phosphorylation at a specific site. The cleidocranial dysplasia in heterozygous *Runx2*-deficient mice was significantly rescued by the genetic insufficiency of GSK-3β or the oral administration of lithium chloride, a selective inhibitor of GSK-3β. These results establish GSK-3β as a key attenuator of Runx2 activity in bone formation and as a potential molecular target for clinical treatment of bone catabolic disorders like cleidocranial dysplasia.

Citation: Kugimiya F, Kawaguchi H, Ohba S, Kawamura N, Hirata M, et al (2007) GSK-3β Controls Osteogenesis through Regulating Runx2 Activity. PLoS ONE 2(9): e837. doi:10.1371/journal.pone.0000837

INTRODUCTION

Bone formation is such a dynamic and intricate process that its perturbation leads to a variety of bone catabolic disorders including skeletal malformations and osteoporosis. Accumulated molecular evidence has revealed the involvements of a number of signalings in this process: Runx2, Wnt, insulin/phosphatidylinositol 3-kinase (PI3K)/Akt, bone morphogenetic proteins/Smads, hedgehog, Osterix, etc [1]. Among them, Runx2 is known to be essential for osteoblastic differentiation, because its null mutation in mice exhibited the complete lack of bone [2–4]. The heterozygous loss leads to cleidocranial dysplasia in both humans and mice, which is attributed to impaired bone formation [4]. Despite accumulated knowledge of these osteogenic siganling molecules, the interactions among them to form the molecular network of bone formation have not been clarified sufficiently to lead to epochal therapeutics to treat bone disorders like cleidocranial dysplasia.

Glycogen synthase kinase-3 (GSK-3) was originally identified as a serine/threonine kinase involved in the regulation of glycogen deposition. The enzyme which comprises two isoforms, GSK-3α and GSK-3β, has since been implicated in many different biological processes including developmental patterning and cell survival as a regulatory switch that integrates numerous signaling pathways [5]. Among them, GSK-3β is known to be a key negative regulator of canonical Wnt/β-catenin and PI3K/Akt signalings [6], both of which have been reported to induce bone formation [7–13]. To investigate the *in vivo* role of GSK-3β, the present study analyzed the skeletal phenotype of GSK-3β-deficient mice, and investigated the underlying molecular mechanism.

RESULTS

Increased bone mass in heterozygous Gsk-3β-deficient mice

To investigate the physiological role of GSK-3β in skeletal tissues, we examined the phenotype of *Gsk-3β*-deficient mice [14]. Although the homozygous *Gsk-3β*-deficient (*Gsk-3β*$^{-/-}$) mice died in late embryogenesis due to severe liver dysfunction, heterozygous *Gsk-3β*-deficient (*Gsk-3β*$^{+/-}$) mice developed and grew normally without disorders in major organs nor gross abnormality in the skeleton (Fig. 1A). However, the radiographs of the entire femurs and the three-dimensional computed tomography (3-D CT) of the distal femurs revealed that *Gsk-3β*$^{+/-}$ mice showed an increased bone mass compared to the wild-type *Gsk-3β*$^{+/+}$ littermates (Fig. 1B, C). Histological examination of the proximal tibiae confirmed the increases in both trabecular and cortical bones without abnormality in the growth plate, indicating that bone metabolism, not cartilage metabolism, was affected by the GSK-3β haploinsufficiency (Fig. 1D). In the bone histomorphometric analysis, the increased trabecular bone volume and cortical thickness in *Gsk-3β*$^{+/-}$ mice were accompanied by significant increases in parameters of bone formation (Fig. 1E). Bone resorption parameters were also enhanced by the GSK-3β insufficiency, although weaker than bone formation parameters (Fig. 1F). Osteoclasts are known to be derived from hematopoietic cells and require cell-cell interactions with osteoblasts or stromal cells for differentiation. In the co-culture of calvarial primary osteoblasts and bone marrow macrophages (BMMϕ), osteoclastogenesis was enhanced when osteoblasts, but not BMMϕ, were derived from *Gsk-3β*$^{+/-}$ mice (Fig. 1G), implicating that the enhanced bone resorption was due to the secondary effect of osteoblast dysfunction, but not the intrinsic defects of osteoclastic cells.

Academic Editor: Carl-Philipp Heisenberg, Max Planck Institute of Molecular Cell Biology and Genetics, Germany

Received May 30, 2007; **Accepted** August 3, 2007; **Published** September 5, 2007

Funding: This study was supported by a Grant-in-aid for Scientific Research from the Japanese Ministry of Education, Culture, Sports, Science, and Technology (#17390410) and Terumo Life Science Foundation. The sponsor had no role in study design, data collection, data analysis, data interpretation, or writing of the manuscript.

Competing Interests: The authors have declared that no competing interests exist.

* **To whom correspondence should be addressed.** E-mail: uichung-tky@umin.ac.jp

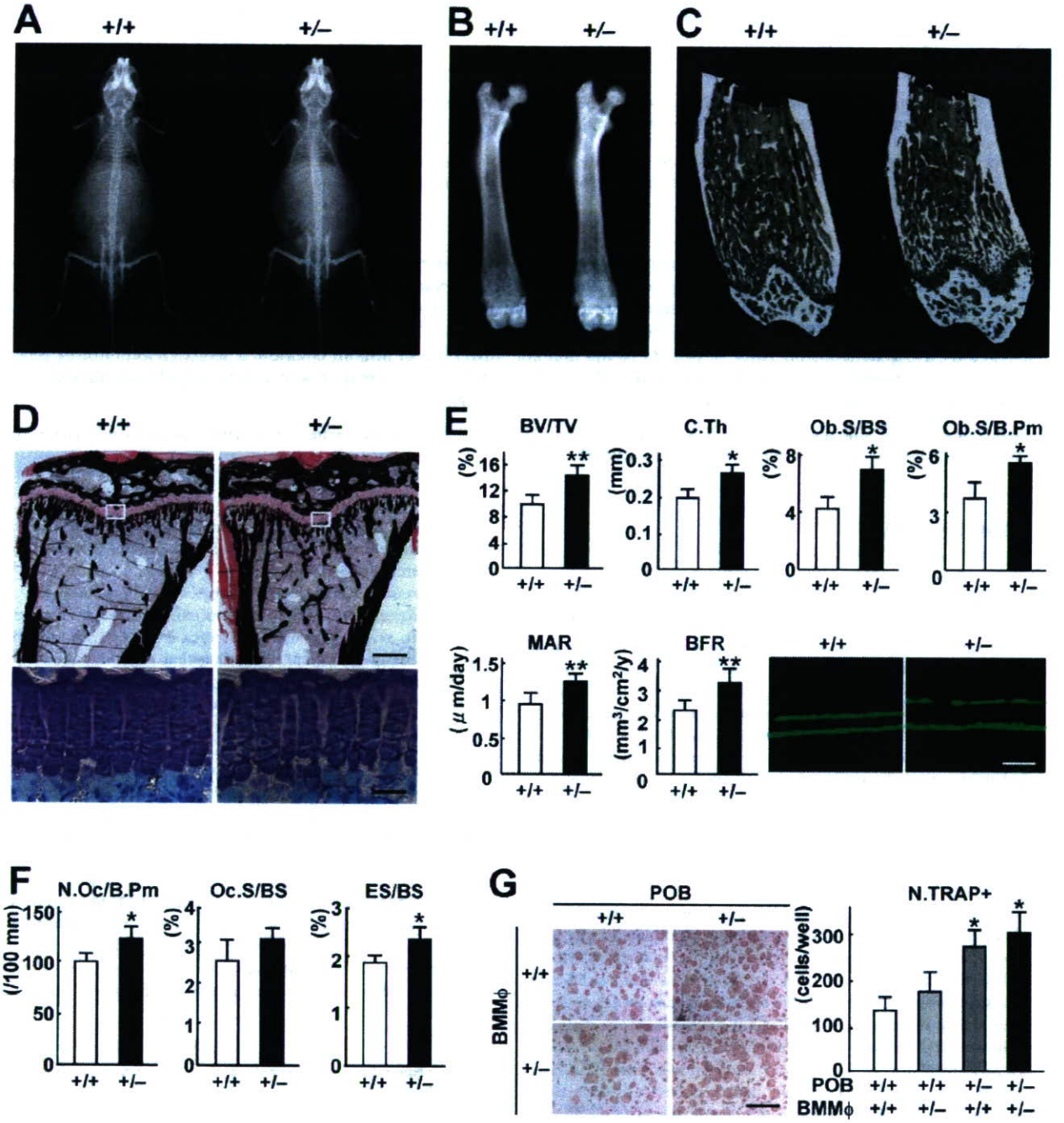

Figure 1. Increased bone mass due to the GSK-3β insufficiency by radiological and histological comparisons of *Gsk-3β*$^{+/+}$ and *Gsk-3β*$^{+/-}$ littermates at 12 weeks of age. (A) Plain X-ray of the whole body. (B) Plain X-ray of the entire femur. (C) 3D-CT image of the distal femur. (D) von Kossa staining of the proximal tibia (bar, 200 μm) and toluidine blue staining of the growth plate indicated by the inset box above (bar, 20 μm). (E) Histomorphometric analyses of bone volume and bone formation parameters in the proximal tibia. BV/TV, trabecular bone volume per tissue volume; C.Th, cortical thickness; Ob.S/BS, osteoblast surface per trabecular bone surface; Ob.S/B.Pm, osteoblast surface per trabecular bone perimeter; MAR, mineral apposition rate; BFR/BS, bone formation rate per trabecular bone surface. Lower right panel shows fluorescent micrographs of calcein-labeled mineralization fronts of the trabecular bones (bar, 10 μm). (F) Histomorphometric analyses of bone resorption parameters in the proximal tibia. N.Oc/B.Pm, number of osteoclasts per 100 mm of bone perimeter; Oc.S/BS, osteoclast surface per bone surface; ES/BS, eroded surface per bone surface. For (E) and (F), data are mean (bars)±SEM (error bars) of 10 mice per genotype. *$P<0.05$, **$P<0.01$ vs. *Gsk-3β*$^{+/+}$. (G) Formation of TRAP-positive multinucleated osteoclasts by the co-culture of calvarial primary osteoblasts (POB) and bone marrow macrophages (BMMϕ) derived from either *Gsk-3β*$^{+/+}$ or *Gsk-3β*$^{+/-}$ mice. Representative pictures (left; bar, 200 μm) and the number of osteoclasts expressed as mean (bars)±SEM (error bars) of 8 wells per group. *$P<0.05$ vs. *Gsk-3β*$^{+/+}$ X *Gsk-3β*$^{+/+}$.

doi:10.1371/journal.pone.0000837.g001

Suppression of bone formation by *GSK-3β* in cultured osteoblasts

To investigate the mechanism underlying the increased bone formation in *Gsk-3β*$^{+/-}$ mice, we compared *ex vivo* cultures of calvarial osteoblasts derived from *Gsk-3β*$^{+/-}$ mice with those from the *Gsk-3β*$^{+/+}$ littermates. The GSK-3β protein level in the *Gsk-3β*$^{+/-}$ osteoblasts was confirmed to be lower than that in the *Gsk-3β*$^{+/+}$, while the GSK-3α level was comparable (Fig. 2A). Although cell proliferation was similar between the two genotypes (Fig. 2B), osteoblast differentiation and function determined by alkaline phosphatase (ALP), Alizarin red, and von Kossa stainings were enhanced in the *Gsk-3β*$^{+/-}$ culture (Fig. 2C). Real-time RT-PCR analyses revealed that expressions of osteoblastic differentiation markers type I collagen (Col I), osteopontin, ALP, and osteocalcin were up-regulated by the GSK-3β insufficiency, whereas the differentiation markers of mesenchymal progenitors Twist-1 and Twist-2 were not affected [15] (Fig. 2D). Overexpression of the wild-type GSK-3β and constitutively active form of GSK-3β (CA-GSK-3β) via the adenoviral introduction significantly suppressed bone formation determined by the von Kossa staining and the osteocalcin mRNA level to similar levels in

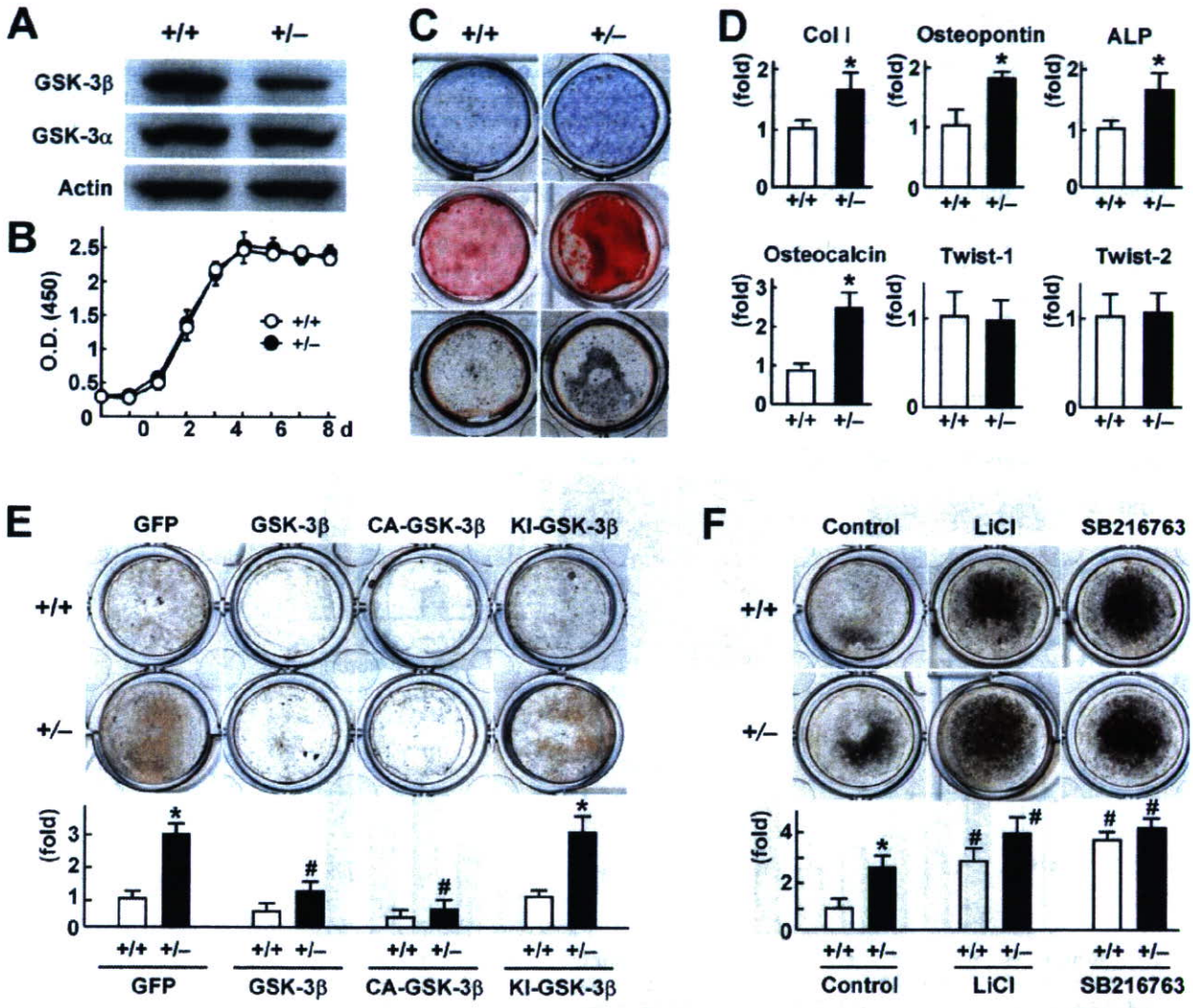

Figure 2. Suppression of bone formation by GSK-3β in cultured osteoblasts. (A) Expressions of GSK-3β and GSK-3α in calvarial osteoblasts of *Gsk-3β*$^{+/+}$ and *Gsk-3β*$^{+/-}$ littermates determined by immunoblot analysis with β-actin as a loading control. (B) Cell proliferation determined by the XTT assay in osteoblasts during 8 days of culture. Data are the mean (symbols) ± SEM (error bars) of 6 dishes/genotype. (C) ALP (top), Alizarin red (middle), and von Kossa (bottom) stainings in osteoblasts cultured for 2 weeks. (D) mRNA levels of type I collagen (Col I), osteopontin, ALP, osteocalcin, Twist-1 and Twist-2, determined by real-time RT-PCR analysis in osteoblasts cultured for 2 weeks. Data are mean (bars) ± SEM (error bars) of the relative amount compared to that of the *Gsk-3β*$^{+/+}$ culture 6 wells per genotype. *$P<0.01$ vs. *Gsk-3β*$^{+/+}$. (E) von Kossa staining (top) and osteocalcin mRNA level determined by real-time RT-PCR analysis (bottom) of osteoblasts transfected with the adenovirus expressing GFP, wild-type GSK-3β, constitutively active GSK-3β (CA-GSK-3β), or kinase-inactive GSK-3β (KI-GSK-3β), and cultured for 2 weeks. (F) von Kossa staining (top) and osteocalcin mRNA level (bottom) of osteoblasts cultured with and without lithium chloride (LiCl, 16 mM) or SB216763 (10 μM) for 2 weeks. For (E) and (F), the mRNA levels are mean (bars) ± SEM (error bars) of the relative amount of mRNA compared to that of the control *Gsk-3β*$^{+/+}$ culture of 6 wells per group. *$P<0.01$, significant stimulation by the genetic GSK-3β insufficiency. #$P<0.01$, significant effects by the adenoviral overexpression or the GSK-3β inhibitors.

doi:10.1371/journal.pone.0000837.g002

the two genotypes; however, overexpression of the kinase-inactive form of GSK-3β (KI-GSK-3β) did not affect it, indicating that kinase activity of GSK-3β is essential for its inhibitory action on bone formation (Fig. 2E). Contrarily, addition of lithium chloride or SB216763, selective inhibitors of GSK-3β, promoted bone formation in the *Gsk-3β*$^{+/+}$ culture to the level similar to the *Gsk-3β*$^{+/}$ culture (Fig. 2F).

Inactivation through phosphorylation of Runx2 by GSK-3β

We next examined the molecular mechanism underlying the GSK-3β inhibition of bone formation. In the two major osteogenic signalings in which GSK-3β is known to be involved, i.e., the canonical Wnt/β-catenin and the PI3K/Akt signalings [5]. A recent *in vivo* study showed that β-catenin hardly affected osteoblasts through a cell-autonomous mechanism [16]. Considering that the other signaling PI3K/Akt is related to Runx2 transactivation in its osteogenic action [17], we examined the involvement of Runx2 in the GSK-3β regulation of bone formation. We initially confirmed both GSK-3β and Runx2 expressions in the calvaria, tibia, and cultured osteoblasts (Fig. 3A). Bone formation determined by von Kossa staining and the osteocalcin mRNA level was enhanced by the Runx2 overexpression in both *Gsk-3β*$^{+/+}$ and *Gsk-3β*$^{+/}$ calvarial osteoblast cultures (Fig. 3B). To examine the regulation of transcriptional activity of Runx2 by GSK-3β, a luciferase reporter gene construct containing a 1,050 bp osteocalcin gene fragment (1,050 OC-Luc) including the Runx2 binding sites was transfected into human hepatoma HuH-7 cells. The luciferase reporter analysis revealed that the Runx2-dependent transcription was suppressed by the co-expression of wild-type GSK-3β and CA-GSK-3β, but not by that of KI-GSK-3β (Fig. 3C), whereas it was enhanced by lithium chloride and SB216763 (Fig. 3D). Collectively, these data demonstrate that the kinase activity of GSK-3β suppresses the Runx2 transcriptional activity.

To further investigate how GSK-3β is involved in the Runx2 activity, we examined the effects of CA-GSK-3β overexpression, lithium chloride treatment, and the genetic GSK-3β insufficiency on the expression and subcellular localization of Runx2, and found that none altered either of them (Fig. 4A). We then transfected *Gsk-3β*$^{+/+}$ and *Gsk-3β*$^{+/}$ osteoblasts with Runx2, and compared the binding of the nuclear extracts with the oligonucleotide probe of the Runx2 binding sequence, osteoblast-specific *cis*-acting element 2 (OSE2) of the mouse *osteocalcin* gene promoter [18], by electrophoretic mobility shift assay (EMSA). We found a complex that was confirmed to represent the Runx2-OSE2 binding, since it diappeared by the addition of 50-fold excess of unlabeled wild-type OSE2 probe, but not by the mutated probe lacking the Runx2 binding sequence, and was undetectable when the nuclear extract from cells without Runx2 transfection was used (Fig. 4B). The specific complex was augmented by the *Gsk-3β*$^{+/}$ nuclear extracts as compared to that by the *Gsk-3β*$^{+/+}$ extracts, indicating that GSK-3β attenuates the DNA binding activity of Runx2. We then investigated biochemical interactions between Runx2 and GSK-3β by co-immunoprecipitation assay, which

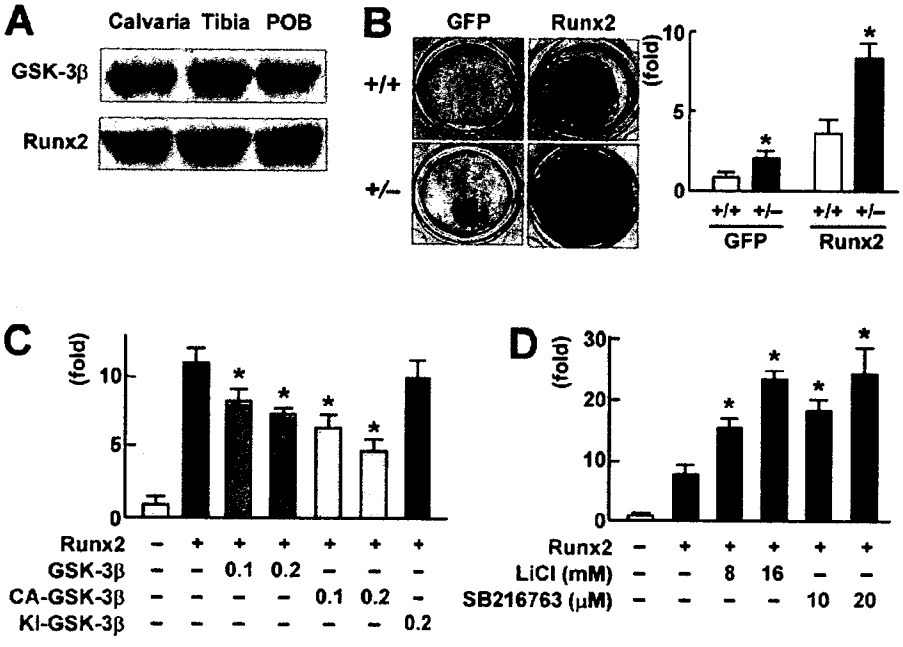

Figure 3. Suppression of Runx2 transcriptional activity by GSK-3β. (A) Expressions of GSK-3β and Runx2 determined by immunoblot analysis in mouse calvaria, tibia, and cultured calvarial primary osteoblasts (POB). (B) von Kossa staining (left) and osteocalcin mRNA level determined by real-time RT-PCR analysis (right) of *Gsk-3β*$^{+/+}$ and *Gsk-3β*$^{+/-}$ osteoblasts transfected with the adenovirus expressing GFP or Runx2, and cultured for 2 weeks. The mRNA levels are mean (bars)±SEM (error bars) of the relative amount of mRNA compared to that of the *Gsk-3β*$^{+/+}$ with GFP culture of 6 wells per group. *$P<0.01$, significant stimulation by the Runx2 overexpression. (C) Luciferase reporter analysis of the effects of GSK-3β overexpression on the Runx2 transcriptional activity. HuH-7 cells were transfected with 1,050 OC-Luc alone or in combination with the plasmid expressing Runx2, and co-transfected with 0.1 or 0.2 μg plasmid expressing wild-type GSK-3β, CA-GSK-3β, or KI-GSK-3β, and cultured for 2 weeks. (D) Luciferase reporter analysis of the effects of GSK-3β inhibitors on the Runx2 transcriptional activity. HuH-7 cells were transfected with 1,050 OC-Luc alone or with the plasmid expressing Runx2, and cultured in the presence or absence of two doses of lithium chloride (LiCl) or SB21673 for 2 days. For (C) and (D), data are mean (bars)±SEM (error bars) of the relative activity compared to control culture of 6 wells per group. *$P<0.01$ vs. Runx2 alone.
doi:10.1371/journal.pone.0000837.g003

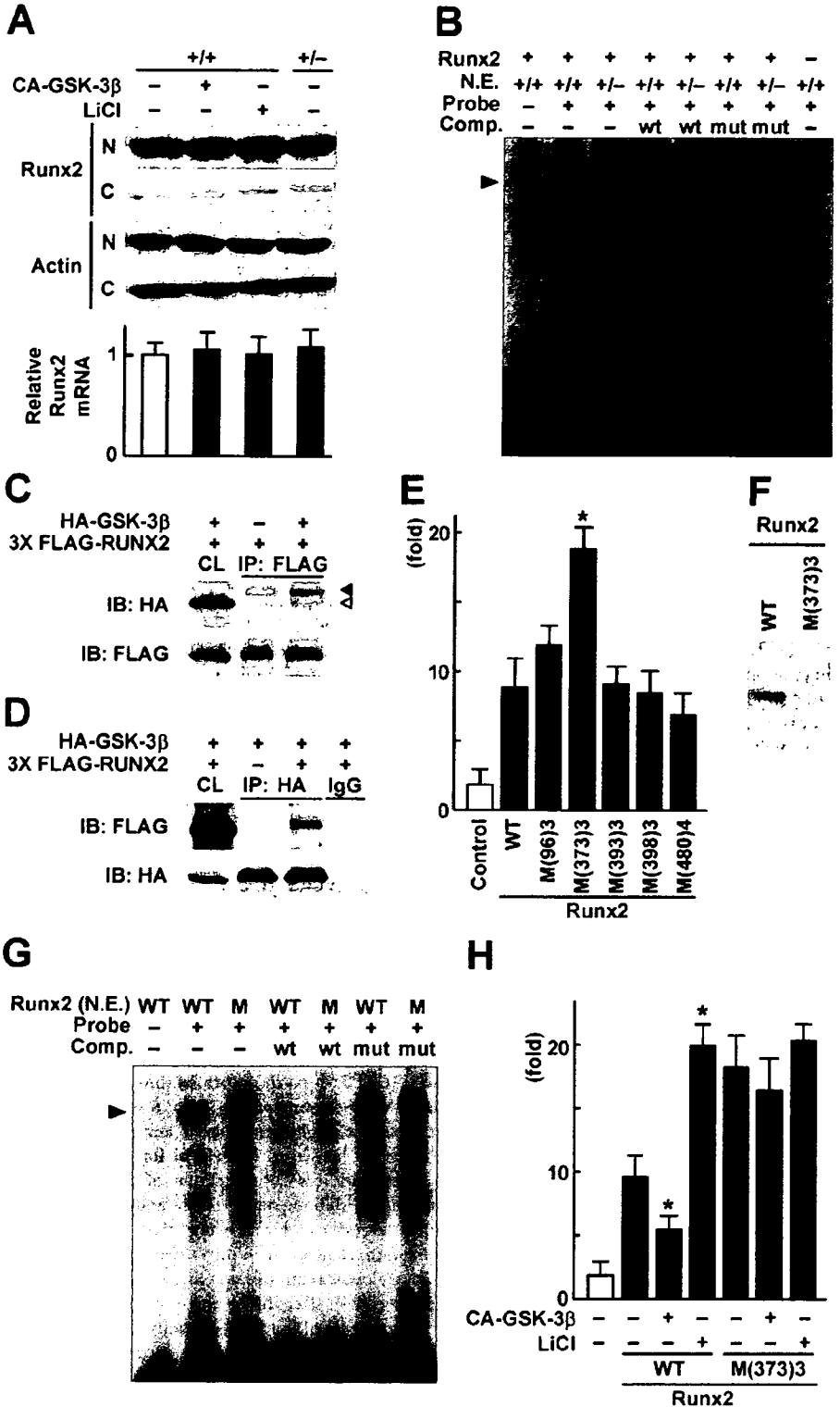

Figure 4. Inactivation through phosphorylation of Runx2 by GSK-3β. (A) Subcellular nuclear (N) and cytoplasmic (C) localizations of Runx2 by immunoblot analysis (top) and Runx2 mRNA level determined by real-time RT-PCR (bottom) in *Gsk-3β*$^{+/+}$ and *Gsk-3β*$^{+/-}$ calvarial osteoblasts overexpressing CA-GSK-3β or treated with LiCl, and cultured for 3 days. The mRNA levels are mean (bars) ± SEM (error bars) of the relative amount compared to the control culture of 6 wells per group. (B) EMSA for specific binding (arrowheads) of a labeled OSE2 oligonucleotide probe with the nuclear extracts (N.E.) from *Gsk-3β*$^{+/+}$ or *Gsk-3β*$^{+/-}$ osteoblasts overexpressing Runx2. Cold competition (Comp.) was performed with 50-fold excess of unlabeled wild-type OSE2 probe (wt) and the mutated probe lacking the Runx2 binding sequence (mut). For controls, incubations without the probe

←

(the 1st lane) and using nuclear extracts from osteoblasts without Runx2 transfection (the last lane) were performed. (C, D) Co-immunoprecipitation (co-IP) analysis of GSK-3b and Runx2. (C) Whole cell lysate (CL) and co-IP precipitant by anti-FLAG antibody-immobilized beads were immunoblotted with either anti-HA tag or anti FLAG tag antibodies. Filled arrowhead indicates non-specific band, and blank arrowhead indicates specific band. (D) Whole cell lysate (CL) and co-IP precipitant by anti-HA tag antibody or IgG (as a negative control) were immunoblotted with either anti-FLAG tag or anti-HA tag antibodies. (E) Luciferase reporter analysis of the effects of Runx2 mutations at the five consensus sites for the phosphorylation by GSK-3β on the Runx2 transcriptional activity. Mutations were created by three to four amino acid replacements as follows; S92A-S96A-S100A [M(96)3], S369A-S373A-S377A [M(373)3], S389A-T393A-S397A [M(393)3], T394A-S398A-T402A [M(398)3], and T476A-T480A-S484A-S488A [M(480)4]. HuH-7 cells were transfected with 1,050 OC-Luc alone or in combination with the plasmids expressing wild-type Runx2 (WT) or the mutants above, then cultured for 2 days. Data are mean (bars)±SEM (error bars) of the relative activity compared to control of 6 wells per group. *$P<0.01$ vs. WT-Runx2. (F) *In vitro* kinase assay. WT-Runx2 and M(373)3-Runx2 proteins were extracted by immunoprecipitation of the overexpresssing HeLa cells, and were incubated with recombinant GSK-3β. Reaction products were analyzed by immunoblotting using an antibody to phosphoserine. (G) EMSA for specific binding (arrowheads) of a labeled OSE2 probe with the nuclear extracts (N.E.) from HeLa cells transfected with wild-type Runx2 (WT) and M(373)3 Runx2 (M). Cold competition (Comp.) was performed as above. (H) Luciferase reporter analysis of the effects of GSK-3β signaling on the Runx2 transcriptional activity induced by WT-Runx2 and M(373)3-Runx2. HuH-7 cells were transfected with 1,050 OC-Luc alone or in combination with the plasmid expressing WT-Runx2 or M(373)3-Runx2 in the presence or absence of CA-GSK-3β overexpression or LiCl, then cultured for 2 days. Data are mean (bars)±SEM (error bars) of the relative activity compared to control of 6 wells per group. *$P<0.01$, significant effect of CA-GSK-3β overexpression or LiCl.
doi:10.1371/journal.pone.0000837.g004

showed the possible direct interaction between these two molecules (Fig. 4C, D). To learn the contribution of the phosphorylation of Runx2 by GSK-3β to the attenuation of Runx2 transcriptional activity, we generated phosphorylation-deficient mutants of Runx2 by creating three to four amino acid replacements at the five consensus sites for the phosphorylation by GSK-3β [5]: S92A-S96A-S100A, S369A-S373A-S377A, S389A-T393A-S397A, T394A-S398A-T402A, and T476A-T480A-S484A-S488A. The luciferase reporter analysis using the 1,050 OC-Luc-transfected HuH-7 cells revealed that the phosphorylation-deficient mutant at S369-S373-S377 enhanced the transcriptional activity, while mutations at the other four phosphorylation sites showed comparable activity to the wild-type Runx2, indicating that the specific phosphorylation at S369-S373-S377 suppresses the Runx2 activity (Fig. 4E). *In vitro* kinase assay confirmed that the Runx2 phosphorylation by GSK-3β was reduced by the S369-S373-S377 mutation (Fig. 4F). When we compared the DNA binding of nuclear extracts from HeLa cells transfected with wild-type and the S369-S373-S377 mutant Runx2 by EMSA, the mutation enhanced the specific Runx2-DNA binding (Fig. 4G). Finally, the luciferase reporter analysis disclosed that the regulations of Runx2-dependent transcription by gain- and loss-of-functions of GSK-3β, i.e., suppression by CA-GSK-3β overexpression and enhancement by lithium chloride, were cancelled by the S369-S373-S377 mutation (Fig. 4H). These lines of results demonstrate that the phosphorylation of Runx2 at S369-S373-S377 by GSK-3β attenuates the transcriptional activity of Runx2, leading to the suppression of bone formation.

Rescue of cleidocranial dysplasia by suppressing GSK-3β

To investigate whether our *in vitro* finding on the molecular interaction between GSK-3β and Runx2 is reproducible *in vivo*, we crossed *Gsk-3*$\beta^{+/-}$ and *Runx2*$^{+/-}$ mice to generate the compound heterozygous deficient mice (*Gsk-3*$\beta^{+/-}$; *Runx2*$^{+/-}$), and analyzed the skeletal phenotypes of neonates. *Runx2*$^{+/-}$ mice, a model for human cleidocranial dysplasia, showed delayed closure of the fontanelle and hypoplasia of the clavicle due to impaired bone formation [3,4], whereas *Gsk-3*$\beta^{+/-}$ mice had no such abnormalities. *Gsk-3*$\beta^{+/-}$; *Runx2*$^{+/-}$ mice exhibited significant rescue of the both fontanelle and clavicle abnormalities of *Runx2*$^{+/-}$ mice (Fig. 5A, B).

Since this finding indicates the physiological interaction of GSK-3β with Runx2 function, we next examined a possible pharmacological intervention by lithium chloride that is reported to inhibit GSK-3β activity both *in vitro* and *in vivo* [19-21]. Because Runx2 is initially detected during embryogenesis at E9.5 in the notochord and at E10.5 in the mesoderm that is destined to develop to the shoulder bones [4], we administered lithium chloride to the embryos through pregnant and lactating dams from E7.5 to 3 weeks of age before weaning. We confirmed that the serum lithium concentrations of the mice treated with this regimen ranged from 0.66 to 0.70 mM, which falls on the lower side of the therapeutic range in humans (0.5–1.5 mM). Here again, the lithium chloride administration succeeded in restoring both fontanelle and clavicle abnormalities in the *Runx2*$^{+/-}$ mice, similarly to the genetic rescue in the *Gsk-3*$\beta^{+/-}$; *Runx2*$^{+/-}$ mice (Fig. 5C, D), raising the possibility that pharmacological intervention such as lithium chloride administration may clinically be useful for preventing cleidocranial dysplasia.

DISCUSSION

GSK-3β as a negative regulator of osteogenesis

The present *in vivo* and *in vitro* studies demonstrated that the suppression of GSK-3β in osteoblasts enhanced bone formation through a cell-autonomous mechanism. GSK-3β is a well-known negative regulator of the canonical Wnt/β-catenin signaling in that it induces proteasome degradation of β-catenin in the absence of the Wnt ligands. Binding of the Wnt ligands to the membrane frizzled receptor and low-density lipoprotein receptor-related protein 5 and 6 (LRP5/6) co-receptors inhibits GSK-3β, causing the stabilization of β-catenin which then translocates into the nucleus to activate the target genes like T cell factor (TCF) [22]. The Wnt signaling is known to be critical for maintaining bone mass, since gain- and loss- of functions of Lrp5 or Wnt10b positively correlated with bone mass in mice and humans [7–9,23]. Furthermore, a recent study showing that lithium chloride increased bone formation even in Lrp5-deficient mice indicates that GSK-3β acts downstream of Lrp5 in the osteogenic action of the Wnt signaling [24]. Regarding the possibility of β-catenin being the target molecule of the GSK-3β action, recent reports on loss- and gain-of-functions of β-catenin have provided compelling evidence that β-catenin represents a differentiation switch of mesenchymal progenitors for inducing osteoblastic differentiation and suppressing chondrocytic differentiation at an early stage of skeletal development during embryogenesis [25–27]. In osteoblastic cells, however, β-catenin together with its target TCF proteins hardly affected their osteogenic function through a cell-autonomous mechanism, but regulated osteoblast expression of osteoprotegerin, a major inhibitor of osteoclast differentiation [16],

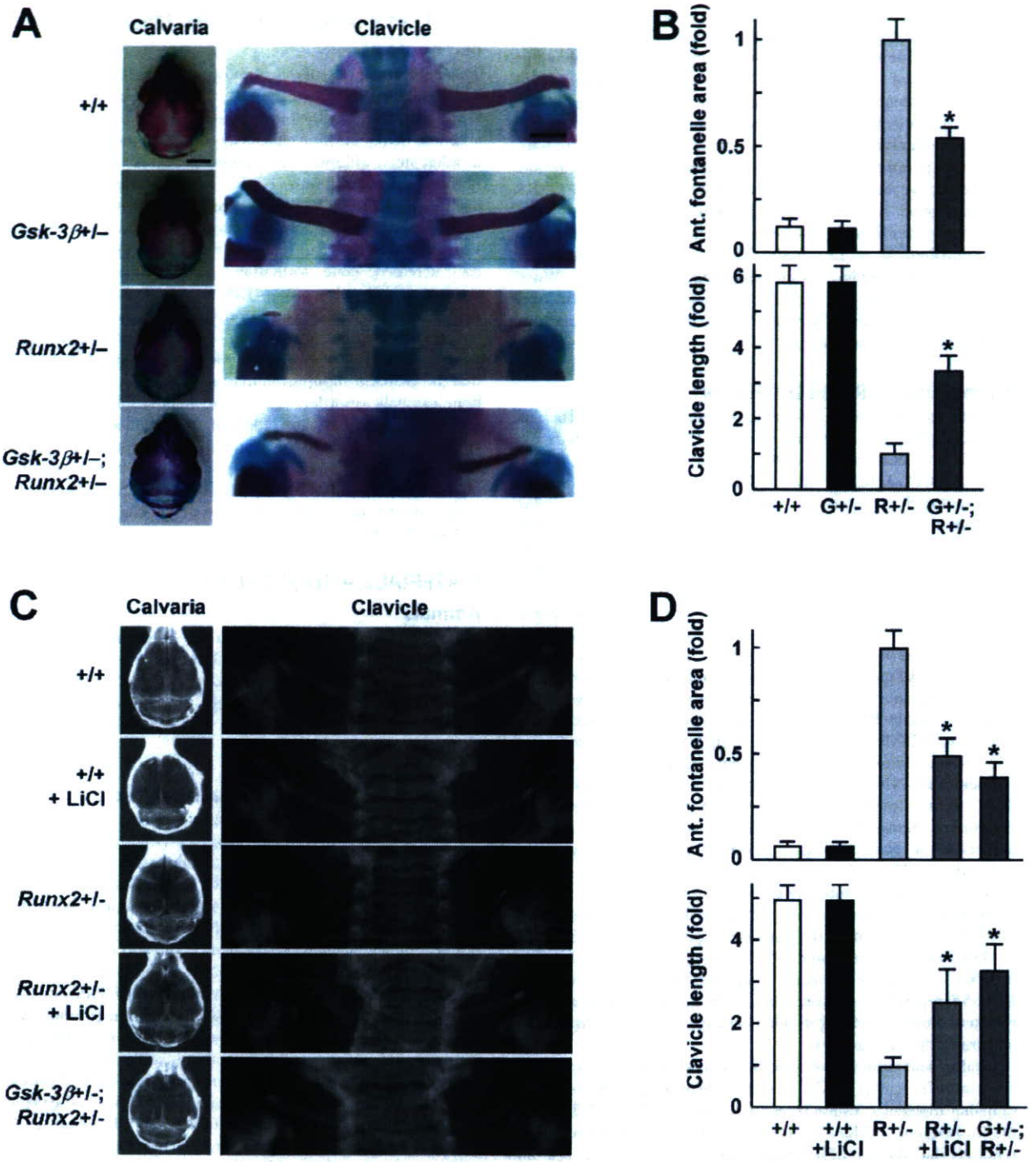

Figure 5. Genetic and pharmacological rescue of cleidocranial dysplasia by suppressing GSK-3β. (A) Calvarias and clavicles of *Gsk-3β*$^{+/+}$, *Gsk-3β*$^{+/-}$, *Runx2*$^{+/-}$, and *Gsk-3β*$^{+/-}$; *Runx2*$^{+/-}$ neonates (0-day) stained with Alizarin red and Alcian blue (bars, 3 mm for calvaria and 0.5 mm for clavicle). (B) Quantitative analyses using the NIH image of the anterior fontanelle area and the clavicle length of the four genotypes. (C) Plain radiographs at 3 weeks of age of the skulls and clavicles of *Gsk-3β*$^{+/+}$ with and without LiCl administration from E7.5 to 3 weeks after birth, *Runx2*$^{+/-}$ with and without the LiCl administration, and *Gsk-3β*$^{+/-}$; *Runx2*$^{+/-}$ mice. (D) Quantitative analyses using the NIH image of the five groups. For (B) and (D), data are mean (bars)±SEM (error bars) of the relative amount compared to *Runx2*$^{+/-}$ of 6 mice per group. *$P<0.01$, significant rescue by genetic GSK-3β insufficiency or LiCl.

doi:10.1371/journal.pone.0000837.g005

indicating that osteoanabolic action of β-catenin is due to the decrease in osteoclastic bone resorption, but not due to the increase in bone formation. Hence, we hereby propose that the enhancement of bone formation by the GSK-3β suppression is mainly dependent on Runx2 rather than β-catenin. In addition, because the histomorphometric analyses of the *Gsk-3β*$^{+/}$ mice and the lithium chloride-treated mice [24] showed an increase in bone formation parameters, but not a decrease in bone resorption parameters, we assume that the bone anabolic action of the GSK-3β suppression is mediated by the Runx2 signaling for bone formation rather than the β-catenin signaling for bone resorption. The contribution and relationship between Runx2 and β-catenin as downstream signalings for the osteoanabolic action of the Wnt/Lrp5 should be further studied to elucidate the cellular and molecular network underlying the regulation of bone metabolism by the entire Wnt pathway.

Attenuation of Runx2 by GSK-3β

A variety of hormones, cytokines and signaling molecules such as $1\alpha,25(OH)_2D_3$, tumor necrosis factor-α, fibroblast growth factor (FGF)-2, glucocorticoids, growth hormone, Akt, Stat1 & 3, Twist, Src/Yes, Dlx3, Msx2, PPARγ, and histone acetylases 3 & 4 have been reported to regulate Runx2 in its expression, subcellular localization, DNA binding, and transcriptional activity, although the mechanisms remain largely unknown [28]. The present study showed that GSK-3β inhibited the DNA binding and transcriptional activity through the S369-S373-S377 phosphorylation of the Runx protein. Regulation of Runx2 activity through its phosphorylation has been reported by phosphorylation-deficient mutagenesis at two conserved serines, S104 and S451 of the human *RUNX2* gene in distinct functional aspects [29]. The S104 phosphorylation is involved in the heterodimerization with the partner subunit PEBP2β, which enhances the transcriptional activity of RUNX2. On the other hand, the phosphorylation of S451 that resides within the C-terminal transcription inhibition domain of RUNX2 attenuates its transactivity. The consensus site T341 for the phosphorylation by PKA in the transactivation domain of mouse Runx2 is shown to be responsible for the induction of Runx2 transcriptional activity by parathyroid hormone (PTH) [30]. In addition, FGF-2 induces the Runx2 activity through phosphorylation of distinct consensus sites of ERK and PKC pathways [31–33]. Meanwhile, the present S369-S373-S377 is located in the negative regulatory region of DNA binding that masks the Runt domain and prevents it from binding to DNA [34]. Hence, the suppression of GSK-3β may relieve the GSK-3β-dependent phosphorylation of the negative regulatory region of Runx2, resulting in enhancement of DNA binding ability and transcriptional activity.

Insulin and insulin-like growth factor-I function as potent osteoanabolic agents [35,36] via the activation of their common signaling molecules insulin receptor substrate (IRS)-1, IRS-2, and the subsequent PI3K/Akt. In fact, we and others previously reported that the loss-of-function mutation of *Irs-1*, *Irs-2*, *or* both *Akt1* and *Akt2* causes impairment of bone formation in mice [11,12,37]. As the target of this pathway, a recent study has shown that Akt enhanced transcriptional activity of Runx2 [17]. However, despite the fact that Akt is a serine-threonine kinase, the study failed to show the direct phosphorylation of Runx2 by Akt, and there was no consensus site for the phosphorylation by Akt in the Runx2 sequence. On the other hand, Akt is known to phosphorylate GSK-3β at Ser9, causing the inactivation [38]. We therefore speculate that the osteoanabolic action of the insulin/IRS/Akt pathway might also be mediated by the Runx2 phosphorylation by GSK-3β.

GSK-3β as a potent therapeutic target for CCD and osteoporosis

The cleidocranial dysplasia phenotype by the Runx2 insufficiency was significantly rescued not only by the genetic suppression of GSK-3β, but also by the oral administration of lithium chloride. In addition, the GSK-3β insufficiency caused an increased bone mass in adult mice without other abnormalities. A previous study has revealed that the lithium chloride administration increased bone mass in normal C57BL/6 mice and osteoporosis model SAMP6 mice [24]. A recent report also showed that oral administration of LY603281-31-8, a small molecule inhibitor of GSK-3β and GSK-3α, increased bone formation, density and strength in an ovariectomized rat model [13] to the levels comparable to teriparatide (human PTH1-34), the only osteoanabolic drug that has recently been introduced into clinical practice for osteoporosis patients [39]. Taken together, these observations strongly suggest that the GSK-3β suppression may yield novel therapeutics to treat bone catabolic disorders like cleidocranial dysplasia and osteoporosis. Although characterization of small molecule inhibitors of GSK-3β is still underway, safety issues have not been reported at least for lithium chloride which is widely used by patients to treat bipolar disorder [40]. Hopefully prospective clinical trials on these drugs will be successful and generate epochal therapeutics for skeletal disorders.

MATERIALS AND METHODS

Animals

Mice were maintained in a C57BL/6 background. In each experiment, male mice that were littermates generated from the intercross between *Gsk-3β*$^{+/+}$ and *Gsk-3β*$^{+/}$ mice were compared. All experiments were performed according to the protocol approved by the Animal Care and Use Committee of the University of Tokyo.

Radiological and histological analyses

Plain radiographs were taken using a soft X-ray apparatus. Micro CT scanning was performed using a composite X-ray analyzer (NS-ELEX Inc.), and cross-sectional tomograms of 10 μm thickness were reconstructed at 12×12 pixels into a 3-D feature by the volume-rending method. For von Kossa and toluidine blue stainings, samples were fixed with 70% ethanol, embedded in glycol methacrylate without decalcification, and sectioned in 3 μm slices. Histomorphometric analyses were performed in the secondary spongiosa (1.0 mm in length from 0.3 mm below the growth plate) of the proximal tibias using an image analyzer. For double labeling to analyze the dynamic bone remodeling, mice were injected subcutaneously with 8 mg/kgBW of calcein at 10 d and 3 d before sacrifice. Tartrate resistant acid phosphatase (TRAP)-positive osteoclasts were stained at pH 5.0 in the presence of L(+)-tartaric acid using naphthol AS-MX phosphate in N,N-dimethyl formamide as the substrate. Histomorphometric measurements were performed in eight optical fields, according to the ASBMR nomenclature report [41], and the averages were calculated per mouse. Alizarin red and alcian blue stainings of the whole mount skeleton of neonates were performed after they were fixed in 100% ethanol and transferred to acetone, as described previously [3]. The specimens were kept in 20% glycerol-1% KOH until the skeletons became clearly visible.

Osteoclast formation assay

Osteoblasts were isolated from calvariae of neonatal mice, and bone marrow cells were collected from long bones of 8-week-old

mice, as previously described [11,12]. TRAP-positive multinucleated osteoclasts were generated by co-culturing osteoblasts (1×10^4 cells/well) and bone marrow cells (5×10^5 cells/well) derived from either *Gsk-3β*$^{+/+}$ or *Gsk-3β*$^{+/-}$ littermates in αMEM containing 10% FBS with $1\alpha,25(OH)_2D_3$ (10 nM) and prostaglandin E_2 (100 nM) for 6 days. Cells positively stained for TRAP and containing more than three nuclei were counted as osteoclasts.

Osteoblast cultures

Isolated calvaria osteoblasts were inoculated at a density of 2×10^5 cells/well onto 24-well plates in αMEM containing 50 μg/ml ascorbic acid, 10 mM β-glycerophosphate, and ITS+1 liquid media supplement (Sigma-Aldrich) (osteogenic medium). For cell proliferation assay, cells were inoculated at 10^3 cells per well in a 96-well plate and cultured for 8 days in the osteogenic medium with cell sampling every day. The proliferation of cells was quantified using an XTT {sodium 3,3-[(phenylamino) carbonyl]-3,4-tetrazolium-bis (4-methoxy-6-nitro) benzenesulfonic acid hydrate} Assay Kit (Roche). The absorbance of the product was quantified using a MTP-300 microplate reader (Corona Electric) read at 450 nm with reference wavelength 630 nm. The adenovirus vector carrying GFP, GSK-3β, CA- GSK-3β, KI-GSK-3β, or Runx2 gene was constructed using the Adeno-X Expression System (BD Biosciences), and was infected at 50 multiplicity of infection (MOI). The total MOI in each well was adjusted to be equal with the adenovirus encoding GFP. Two weeks after confluency, the total RNA was extracted, and the ALP, Alizarin red and von Kossa stainings were performed. For the ALP staining, cells were fixed in 70% ethanol and stained for 10 min with a solution containing 0.01% naphtol AS-MX phosphate disodium salt, 1% N, N-dimethyl-formamide, and 0.06% fast blue BB. For the Alizarin red staining, cells were fixed in 10% formalin/PBS and stained with 2% Alizarin red S (pH 4.0) solution. For the von Kossa staining, cells were fixed with 100% ethanol, stained with 5% silver nitrate solution under ultraviolet light, and incubated with 5% sodium thiosulfate solution (Wako).

Real-time RT-PCR

The total RNA was extracted using an ISOGEN Kit (Wako) and an RNeasy Mini Kit (QIAGEN), and treated with DNaseI (QIAGEN), according to the manufacturers' instructions. One μg of RNA was reverse-transcribed with a Takara RNA PCR Kit (AMV) ver.2.1 (Takara) to generate single-stranded cDNA. PCR was performed with an ABI Prism 7000 Sequence Detection System (Applied Biosystems). Each PCR reaction consisted of 1 X QuantiTect SYBR Green PCR Master Mix (QIAGEN), 0.3 μM specific primers and 500 ng of cDNA. The mRNA copy number of a specific gene in total RNA was calculated using a standard curve generated by serially diluted plasmids containing PCR amplicon sequences, and normalized to the human or rodent total RNA (Applied Biosystems) with the mouse actin as an internal control. The standard plasmids were synthesized using a TOPO TA Cloning Kit (Invitrogen), according to manufacturer's instructions. All reactions were run in triplicate. Primer sequences are available upon request.

Immunoblot and immunoprecipitation assays

Proteins were extracted with an M-PER or NE-PER Kit (Pierce Chemical), according to the manufacturer's instructions. Protein concentrations of cell lysates were measured using a Protein Assay Kit II (BIO-RAD). For immunoblot analysis, lysates were fractionated by SDS-PAGE with 4-20% Tris-Glycin gradient gel or 18% Tris-Glycin gel (Invitrogen) and transferred onto nitrocellulose membranes (BIO-RAD). After being blocked with 6% milk/TBS-T, membranes were incubated with an antibody to GSK-3α (Cell Signaling), to GSK-3β (Cell Signaling), to Runx2 (MBL), to HA tag (Upstate), to FLAG tag (Sigma-Aldrich), or to β-actin (Sigma-Aldrich). As secondary antibodies, HRP-conjugated antibodies to mouse IgG (Promega) and to rabbit IgG (Promega) were used. Immunoreactive bands were visualized with ECL Plus (Amersham), according to the manufacturer's instructions. Immunoprecipitation was performed using antibodies either noncovalently bound or conjugated to protein G-Sepharose (GIBCO). Equivalent amounts (20 μg) of cell lysate were immunoprecipitated with an antibodyb to Runx2 for 4 hours at 4°C. For co-immunoprecipitation (co-IP), cDNA encoding RUNX2 and GSK-3β genes were sub-cloned into p3XFLAG-CMV™ (Sigma-Aldrich) vector (3X FLAG-RUNX2) and pCMV-HA (Clontech) vector (HA-GSK-3β), respectively. Supernatant of centrifuged cell lysate, collected using RIPA lysis buffer (150 mM NaCl, 1.0% NP-40, 0.5% sodium deoxycholate, 0.1% sodium dodecyl sulfate, 50 mM Tris, pH 8.0) from 293T cells transfected with 3X FLAG-RUNX2 and/or HA-GSK-3β, was subjected to subsequent analysis. The co-IP complexes were recovered using EZview™ Red ANTI-FLAG® M2 Affinity Gel (Sigma-Aldrich) or Pro-Found™ HA Tag IP/Co-IP Kit (Pierce) according to the manufacturer's instruction.

Luciferase reporter analysis and EMSA

Huh-7 cells were plated onto 24-well plates, and were transfected with 0.1 μg of the reporter constructs (1,050 OC-Luc) and 0.1 or 0.2 μg of the plasmids encoding wild-type or five kinds of phosphorylation-deficient mutants of Runx2, GSK-3β, CA-GSK-3β, or KI-GSK-3β using FuGENE6 (Roche Diagnostics), and cultured for 2 days. The amount of total DNA in each well was adjusted to be equal with the pEGFP vector. The luciferase assay was performed using a PicaGene Dual SeaPansy Luminescence Kit (Toyo Ink) and Lumat LB 9507 (Berthold Technologies). The level of luciferase activity was normalized to the level of Renilla luciferase activity. EMSA was performed using a DIG Gel Shift Kit (Roche), according to the manufacturer's instructions. In brief, nuclear extracts from *Gsk-3β*$^{+/+}$ or *Gsk-3β*$^{+/-}$ osteoblasts transfected with plasmid expressing wild-type Runx2, or HeLa cells transfected with wild-type or M(373)3 Runx2 were incubated with digoxigenin-labeled double-stranded oligo-dNT probes encoding the OSE2 sequence [18] and separated using non-denaturing PAGE, and the immunoreactivity for digoxigenin was visualized by chemiluminescence. For the competition experiment, 50-fold excess of unlabelled wild-type or the mutated OSE2 probe was added to the solution.

In vitro kinase assay

Flag-wild-type Runx2 or Flag-M(373)3 Runx2 was prepared from the respective Runx2 overexpresssing HeLa cells by immunoprecipitation with an antibody to Flag. The immunoprecipitated protein and recombinant human GSK-3β (Upstate) were mixed in a reaction buffer (20 mM HEPES, 10 mM $MgCl_2$, 10 mM $MnCl_2$, 1 mM dithiothreitol, and 0.2 mM EDTA) with 1.6 mM ATP, and incubated at 30°C for 30 min. Reaction products were analyzed by immunoblotting using an antibody to phosphoserine (CHEMICON).

Rescue of cleidocranial dysplasia by suppressing GSK-3β

Runx2$^{+/-}$ mice were kindly provided by T. Komori (Nagasaki University). For the genetic rescue, we crossed *Gsk-3β*$^{+/-}$ and

Runx2$^{+/-}$ mice to generate the compound heterozygous deficient mice (*Gsk-3β*$^{+/-}$; *Runx2*$^{+/-}$), and compared the skeletal phenotypes of neonates with *Runx2*$^{+/-}$. For the pharmacological rescue, we administered lithium chloride from E7.5 to 3 weeks of age before weaning through the pregnant and lactating dams by feeding with pelleted chow containing 4 mg/kg lithium chloride along with 1.5% NaCl water as previously described [20,21]. The mice were euthanized for radiological analyses at 3 weeks. The quantitative analysis of the area of the anterior fontanelles and the length of the clavicles on the histology and X-ray were performed using an NIH Image. The serum lithium concentration of the treated mice was measured by an atomic absorption spectrophotometer (Hitachi).

Statistical analysis

All data are means±SEMs. Means of groups were compared by ANOVA and significance of differences was determined by *post-hoc* testing using Bonferroni's method.

ACKNOWLEDGMENTS

We thank T. Komori for *Runx2*$^{+/-}$ mice, and K. Miyazono and J. Lian for providing DNA constructs.

Author Contributions

Conceived and designed the experiments: HK FK UC. Performed the experiments: NK FK SO MH. Analyzed the data: FK KN. Contributed reagents/materials/analysis tools: JW NK SO HC YA. Wrote the paper: FK.

REFERENCES

1. Karsenty G, Wagner EF (2002) Reaching a genetic and molecular understanding of skeletal development. Dev Cell 2: 389–406.
2. Ducy P, Zhang R, Geoffroy V, Ridall AL, Karsenty G (1997) Osf2/Cbfa1: a transcriptional activator of osteoblast differentiation. Cell 89: 747–754.
3. Komori T, Yagi H, Nomura S, Yamaguchi A, Sasaki K, et al. (1997) Targeted disruption of Cbfa1 results in a complete lack of bone formation owing to maturational arrest of osteoblasts. Cell 89: 755–764.
4. Otto F, Thornell AP, Crompton T, Denzel A, Gilmour KC, et al. (1997) Cbfa1, a candidate gene for cleidocranial dysplasia syndrome, is essential for osteoblast differentiation and bone development. Cell 89: 765–771.
5. Doble BW, Woodgett JR (2003) GSK-3: tricks of the trade for a multi-tasking kinase. J Cell Sci 116: 1175–1186.
6. Patel S, Doble B, Woodgett JR (2004) Glycogen synthase kinase-3 in insulin and Wnt signalling: a double-edged sword? Biochem Soc Trans 32: 803–808.
7. Gong Y, Slee RB, Fukai N, Rawadi G, Roman-Roman S, et al. (2001) LDL receptor-related protein 5 (LRP5) affects bone accrual and eye development. Cell 107: 513–523.
8. Kato M, Patel MS, Levasseur R, Lobov I, Chang BH, et al. (2002) Cbfa1-independent decrease in osteoblast proliferation, osteopenia, and persistent embryonic eye vascularization in mice deficient in Lrp5, a Wnt coreceptor. J Cell Biol 157: 303–314.
9. Boyden LM, Mao J, Belsky J, Mitzner L, Farhi A, et al. (2002) High bone density due to a mutation in LDL-receptor-related protein 5. N Engl J Med 346: 1513–1521.
10. Little RD, Carulli JP, Del Mastro RG, Dupuis J, Osborne M, et al. (2002) A mutation in the LDL receptor-related protein 5 gene results in the autosomal dominant high-bone-mass trait. Am J Hum Genet 70: 11–19.
11. Ogata N, Chikazu D, Kubota N, Terauchi Y, Tobe K, et al. (2000) Insulin receptor substrate-1 in osteoblast is indispensable for maintaining bone turnover. J Clin Invest 105: 935–943.
12. Akune T, Ogata N, Hoshi K, Kubota N, Terauchi Y, et al. (2002) Insulin receptor substrate-2 maintains predominance of anabolic function over catabolic function of osteoblasts. J Cell Biol 159: 147–156.
13. Krishnan V, Bryant HU, Macdougald OA (2006) Regulation of bone mass by Wnt signaling. J Clin Invest 116: 1202–1209.
14. Hoeflich KP, Luo J, Rubie EA, Tsao MS, Jin O, et al. (2000) Requirement for glycogen synthase kinase-3beta in cell survival and NF-kappaB activation. Nature 406: 86–90.
15. Bialek P, Kern B, Yang X, Schrock M, Sosic D, et al. (2004) A twist code determines the onset of osteoblast differentiation. Dev Cell 6: 423–435.
16. Glass DA 2nd, Bialek P, Ahn JD, Starbuck M, Patel MS, et al. (2005) Canonical Wnt signaling in differentiated osteoblasts controls osteoclast differentiation. Dev Cell 8: 751–764.
17. Fujita T, Azuma Y, Fukuyama R, Hattori Y, Yoshida C, et al. (2004) Runx2 induces osteoblast and chondrocyte differentiation and enhances their migration by coupling with PI3K-Akt signaling. J Cell Biol 166: 85–95.
18. Ducy P, Karsenty G (1995) Two distinct osteoblast-specific cis-acting elements control expression of a mouse osteocalcin gene. Mol Cell Biol 15: 1858–1869.
19. Davies SP, Reddy H, Caivano M, Cohen P (2000) Specificity and mechanism of action of some commonly used protein kinase inhibitors. Biochem J 351: 95–105.
20. Dixon JF, Hokin LE (1998) Lithium acutely inhibits and chronically up-regulates and stabilizes glutamate uptake by presynaptic nerve endings in mouse cerebral cortex. Proc Natl Acad Sci U S A 95: 8363–8368.
21. De Sarno P, Li X, Jope RS (2002) Regulation of Akt and glycogen synthase kinase-3 beta phosphorylation by sodium valproate and lithium. Neuropharmacology 43: 1158–1164.
22. Westendorf JJ, Kahler RA, Schroeder TM (2004) Wnt signaling in osteoblasts and bone diseases. Gene 341: 19–39.
23. Bennett CN, Longo KA, Wright WS, Suva LJ, Lane TF, et al. (2005) Regulation of osteoblastogenesis and bone mass by Wnt10b. Proc Natl Acad Sci U S A 102: 3324–3329.
24. Clement-Lacroix P, Ai M, Morvan F, Roman-Roman S, Vayssiere B, et al. (2005) Lrp5-independent activation of Wnt signaling by lithium chloride increases bone formation and bone mass in mice. Proc Natl Acad Sci U S A 102: 17406–17411.
25. Day TF, Guo X, Garrett-Beal L, Yang Y (2005) Wnt/beta-catenin signaling in mesenchymal progenitors controls osteoblast and chondrocyte differentiation during vertebrate skeletogenesis. Dev Cell 8: 739–750.
26. Hill TP, Spater D, Taketo MM, Birchmeier W, Hartmann C (2005) Canonical Wnt/beta-catenin signaling prevents osteoblasts from differentiating into chondrocytes. Dev Cell 8: 727–738.
27. Hu H, Hilton MJ, Tu X, Yu K, Ornitz DM, et al. (2005) Sequential roles of Hedgehog and Wnt signaling in osteoblast development. Development 132: 49–60.
28. Komori T (2005) Regulation of skeletal development by the Runx family of transcription factors. J Cell Biochem 95: 445–453.
29. Wee HJ, Huang G, Shigesada K, Ito Y (2002) Serine phosphorylation of RUNX2 with novel potential functions as negative regulatory mechanisms. EMBO Rep 3: 967–974.
30. Selvamurugan N, Pulumati MR, Tyson DR, Partridge NC (2000) Parathyroid hormone regulation of the rat collagenase-3 promoter by protein kinase A-dependent transactivation of core binding factor alpha1. J Biol Chem 275: 5037–5042.
31. Xiao G, Jiang D, Thomas P, Benson MD, Guan K, et al. (2000) MAPK pathways activate and phosphorylate the osteoblast-specific transcription factor, Cbfa1. J Biol Chem 275: 4453–4459.
32. Xiao G, Jiang D, Gopalakrishnan R, Franceschi RT (2002) Fibroblast growth factor 2 induction of the osteocalcin gene requires MAPK activity and phosphorylation of the osteoblast transcription factor, Cbfa1/Runx2. J Biol Chem 277: 36181–36187.
33. Kim BG, Kim HJ, Park HJ, Kim YJ, Yoon WJ, et al. (2006) Runx2 phosphorylation induced by fibroblast growth factor-2/protein kinase C pathways. Proteomics 6: 1166–1174.
34. Ito Y (1999) Molecular basis of tissue-specific gene expression mediated by the runt domain transcription factor PEBP2/CBF. Genes Cells 4: 685–696.
35. Canalis E (1993) Insulin like growth factors and the local regulation of bone formation. Bone 14: 273–276.
36. Thrailkill KM, Lumpkin CK Jr, Bunn RC, Kemp SF, Fowlkes JL (2005) Is insulin an anabolic agent in bone? Dissecting the diabetic bone for clues. Am J Physiol Endocrinol Metab 289: E735–745.
37. Peng XD, Xu PZ, Chen ML, Hahn-Windgassen A, Skeen J, et al. (2003) Dwarfism, impaired skin development, skeletal muscle atrophy, delayed bone development, and impeded adipogenesis in mice lacking Akt1 and Akt2. Genes Dev 17: 1352–1365.
38. Cross DA, Alessi DR, Cohen P, Andjelkovich M, Hemmings BA (1995) Inhibition of glycogen synthase kinase-3 by insulin mediated by protein kinase B. Nature 378: 785–789.
39. Neer RM, Arnaud CD, Zanchetta JR, Prince R, Gaich GA, et al. (2001) Effect of parathyroid hormone (1-34) on fractures and bone mineral density in postmenopausal women with osteoporosis. N Engl J Med 344: 1434–1441.
40. Cohen Y, Chetrit A, Sirota P, Modan B (1998) Cancer morbidity in psychiatric patients: influence of lithium carbonate treatment. Med Oncol 15: 32–36.
41. Parfitt AM, Drezner MK, Glorieux FH, Kanis JA, Malluche H, et al. (1987) Bone histomorphometry: standardization of nomenclature, symbols, and units. Report of the ASBMR Histomorphometry Nomenclature Committee. J Bone Miner Res 2: 595–610.

Bone Regeneration by Regulated *In Vivo* Gene Transfer Using Biocompatible Polyplex Nanomicelles

Keiji Itaka[1], Shinsuke Ohba[1], Kanjiro Miyata[2], Hiroshi Kawaguchi[3], Kozo Nakamura[3], Tsuyoshi Takato[3], Ung-Il Chung[1] and Kazunori Kataoka[1,2]

[1]*Division of Clinical Biotechnology, Center for Disease Biology and Integrative Medicine, Graduate School of Medicine, The University of Tokyo, Tokyo, Japan;* [2]*Department of Materials Science and Engineering, Graduate School of Engineering, The University of Tokyo, Tokyo, Japan;* [3]*Division of Sensory and Motor System Medicine, Faculty of Medicine, The University of Tokyo, Tokyo, Japan*

Gene therapy is a promising strategy for bone regenerative medicine. Although viral vectors have been intensively studied for delivery of osteogenic factors, the immune response inevitably inhibits bone formation. Thus, safe and efficient non-viral gene delivery systems are in high demand. Toward this end, we developed a polyplex nanomicelle system composed of poly(ethyleneglycol) (PEG)-block-catiomer (PEG-b-P[Asp-(DET)]) and plasmid DNA (pDNA). This system showed little cytotoxicity and excellent transfection efficiency to primary cells. By the transfection of constitutively active form of activin receptor-like kinase 6 (caALK6) and runt-related transcription factor 2 (Runx2), the osteogenic differentiation was induced on mouse calvarial cells to a greater extent than when poly(ethylenimine) (PEI) or FuGENE6 were used; this result was due to low cytotoxicity and a sustained gene expression profile. After incorporation into the calcium phosphate cement scaffold, the polyplex nanomicelles were successfully released from the scaffold and transfected surrounding cells. Finally, this system was applied to *in vivo* gene transfer for a bone defect model in a mouse skull bone. By delivering *caALK6* and *Runx2* genes from nanomicelles incorporated into the scaffold, substantial bone formation covering the entire lower surface of the implant was induced with no sign of inflammation at 4 weeks. These results demonstrate the first success in *in vivo* gene transfer with therapeutic potential using polyplex nanomicelles.

Received 31 December 2006; accepted 30 April 2007; advance online publication 5 June 2007; doi:10.1038/sj.mt.6300218

INTRODUCTION

Despite bone's capacity to heal spontaneously, bone repair is not always satisfactory. Approximately 5–10% of fractures do not heal well, resulting in delayed union or non-union with considerable morbidity.[1] Critical bone defects after severe trauma, tumor resection, or revision of total joint arthroplasty remain challenging problems. Autologous bone graft is considered the gold standard technique; however, it has shortcomings concerning both quantity (availability of material) and quality (donor site troubles, graft rejection, disease transmission).[2,3] These problems have heightened the need for bone regenerative medicine that uses tissue engineering techniques.[4]

A promising strategy is to combine adequate scaffolds and signals. Although some scaffolds are osteoconductive, no scaffolds invented so far are known to be osteoinductive,[5] because current scaffold materials cannot activate the signals necessary for osteogenesis. For this purpose, the potential of growth and transcriptional factors has been widely recognized.[6,7] Substantial progress has been made in the basic understanding of major osteogenic signaling molecules such as bone morphogenetic proteins (BMPs),[8] Hedgehogs,[9] Runx2,[10] Wnts,[11] and insulin-like growth factors.[12] In particular, recombinant human BMP-2 and BMP-7 have already been approved by the U.S. Food and Drug Administration for restricted clinical use. However, in spite of the remarkable findings on animal studies, clinical trials using BMP devices have not obtained comparable outcomes.[13,14] Problems such as protein stability, inadequate release profile (initial burst effect), or the need for accessory factors may have caused these inconsistent results.[6,15]

Gene therapy is a promising approach to overcome these problems. Compared with exogenous proteins, which require purification, the gene can express these bioactive factors in the native form at the regeneration site.[6] The sustained synthesis of proteins from the delivered gene can facilitate synchronization between the kinetics of signaling receptor expression and bioactive factor availability.[16] In addition, the combined use of two or more osteoinductive factors to constitute a better osteogenic signal can be evaluated with a high degree of flexibility.[17] For this purpose, viral vectors including adenovirus and adeno-associated virus vectors have been intensively studied for the delivery of the osteoinductive cytokines.[17–21] However, when these viral vectors are used, there is concern about inducing immune responses.[22] Indeed, Egermann *et al.* reported that, after a local injection of BMP-2 expressing adenoviral vector to a bone defect area in sheep, bone formation was significantly reduced even at the untreated contralateral defect area, indicating that the immune

The first two authors contributed equally to this work.

Correspondence: *Kazunori Kataoka, Department of Materials Science and Engineering, Graduate School of Engineering, The University of Tokyo, 7-3-1 Hongo, Bunkyo-ku, Tokyo 113-0033, Japan. E-mail: kataoka@bmw.t.u-tokyo.ac.jp*

response has a systemic inhibitory effect on bone formation after a single injection of adenovirus.[23]

In this context, safe and efficient non-viral gene delivery systems are in high demand. We recently developed a novel polymer-based gene delivery system that showed excellent capacity for *in vitro* transfection.[24] This system is a polyplex nanomicelle composed of poly(ethyleneglycol) (PEG)-block-polycation (PEG-b-P[Asp-(DET)]): PEG-b-polyasparagine carrying the *N*-(2-aminoethyl)aminoethyl group $(CH_2)_2NH(CH_2)_2NH_2$ as the side chain) and plasmid DNA (pDNA). The complexation of block copolymer and pDNA forms a micellar structure, and its characteristics have been found suitable for gene delivery: a diameter of ~100 nm with a PEG palisade enabling complexes to avoid foreign body recognition while providing increased nuclease resistance, increased tolerance under physiologic conditions, and excellent gene expression in a serum-containing medium.[25–27] In addition, the cationic segment of block copolymer was designed to have the buffering capacity of an acidic environment inside the endosomes as effected by the presence of unprotonated amines under neutral pH. By virtue of these features, we effectively transfected genes to culture cells with almost no cytotoxicity.[24]

We undertook the present study to investigate the feasibility of these polyplex nanomicelles for bone regenerative medicine, including the study of: (i) transfection toward various primary cells for the evaluation of efficiency and safety, (ii) induction of osteogenic differentiation by a foreign gene introduction of osteogenic factors, and (iii) *in vivo* gene transfer to a mouse bone defect model to increase the rate of bone regeneration. As will be shown, this system provides sufficient gene expression in a sustained manner both *in vitro* and *in vivo*, and it thus shows a potential therapeutic effect in a bone defect model.

RESULTS

In vitro transfection to human synovial cells

To evaluate the feasibility of polyplex nanomicelles for clinical gene therapy, *in vitro* transfection was performed toward human synovial cells derived from patients suffering from rheumatoid arthritis. By evaluating luciferase gene expression on day 2 of transfection, the polyplex nanomicelles that were formed at an optimal nitrogen/phosphate ratio showed gene expressions comparable to those of linear poly(ethylenimine) (LPEI),[28] which is well known to have excellent transfection efficiency (**Figure 1a**). At the optimal nitrogen/phosphate = 80, the polyplex nanomicelles were observed to have small absolute zeta potentials of around +10 mV (**Supplementary Figure S1**). The nanomicelles maintained appreciable gene expression even on day 5, whereas the gene expression of LPEI showed a marked decrease during the same time frame. To investigate this difference, the cytotoxicity was evaluated by a quantitative assay. Consistent with the results of gene expression, LPEI exhibited prominent cytotoxicity time-dependently (**Figure 1b**). The microscopic images following green fluorescence protein (GFP) gene transfection by LPEI showed apparent morphologic change as well as reduced numbers of cells, whereas the polyplex nanomicelles maintained almost normal phenotype concurrently with GFP expression even on day 5 (**Supplementary Figure S2**). Thus, the polyplex

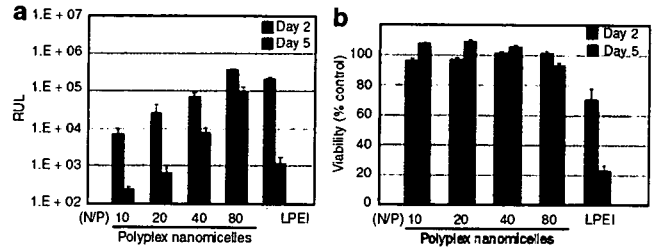

Figure 1 *In vitro* transfection to human synovial cells. (**a**) Luciferase gene expression. *In vitro* transfection of luciferase-expressing plasmid DNA was performed by polyplex nanomicelles formed at various nitrogen/phosphate (N/P) ratios and by poly(ethylenimine) (LPEI). Gene expression was evaluated after 2 and 5 days of transfection. Data are means ± SDs, $n = 4$. (**b**) Cell viability after transfection. After transfection, similar to the case in **a**, cell viability was estimated by an MTT assay. Results were expressed as the relative value (%) of the control cells, which were incubated in parallel without transfection. Data are means ± SDs, $n = 8$. RLU, relative light units.

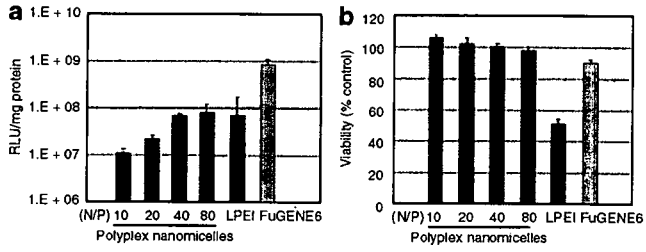

Figure 2 *In vitro* transfection to mouse calvarial cells. (**a**) Luciferase gene expression. *In vitro* transfection of luciferase-expressing plasmid DNA was performed using polyplex nanomicelles, formed at various nitrogen/phosphate (N/P) ratios, as well as poly(ethylenimine) (LPEI) and FuGENE6. Gene expression was evaluated after 2 days of transfection. Data are means ± SDs, $n = 4$. (**b**) Cell viability after transfection. After transfection, similar to the case in **a**, cell viability was estimated by an MTT assay. Results were expressed as relative values (%) of the control cells, which were incubated in parallel without transfection. Data are means ± SDs, $n = 8$. RLU, relative light units.

nanomicelles were revealed to have excellent gene transfection capacity—comparable to that of LPEI—with considerably low cytotoxicity; this suggests a great advantage for *in vivo* application.

Transfection toward mouse calvarial cells and induction of osteogenic differentiation

In applying polyplex nanomicelles to delivery genes encoding bioactive factors that activate signals necessary for osteogenesis, we evaluated the transfection capacity of foreign genes and the induction of cell differentiation toward mouse calvarial cells derived from neonatal calvariae. The evaluation of luciferase showed that gene expressions comparable to those of LPEI were obtained by polyplex nanomicelles (**Figure 2a**) without showing any cytotoxicity (**Figure 2b**). From a practical standpoint we also evaluated FuGENE6, a commercially available lipid-based transfection reagent with considerably high efficiency and biocompatibility.[29–33] With this reagent, the cells showed luciferase expression that was one order higher than with polyplex nanomicelles or LPEI and with little cytotoxicity (**Figure 2a** and **b**).

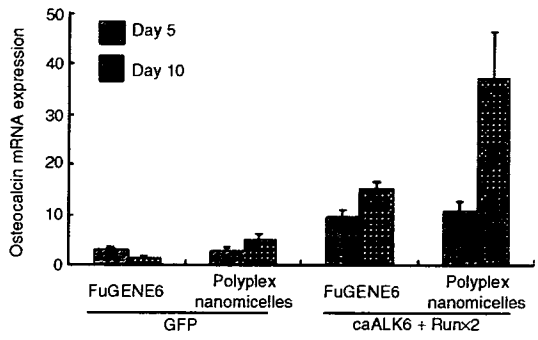

Figure 3 Evaluation of osteocalcin messenger RNA (mRNA) expression by a quantitative polymerase chain reaction (PCR). Osteogenic differentiation was induced on the mouse calvarial cells by transfection of caALK6 and Runx2 expressing plasmid DNAs. As a negative control, a green fluorescence protein (GFP) gene was also used. After 5 and 10 days, the total RNA was collected and the osteocalcin expression was quantified by a quantitative PCR. Data are means ± SDs, $n = 6$. caALK6, constitutively active form of activin receptor-like kinase 6; Runx2, runt-related transcription factor 2.

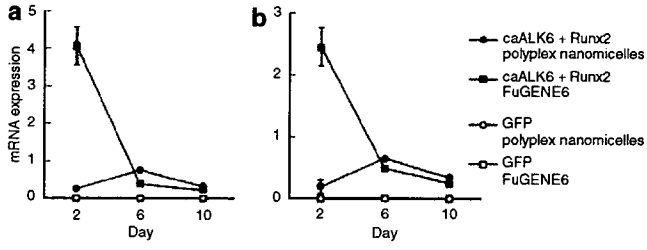

Figure 4 Evaluation of messenger RNA (mRNA) expression of (**a**) constitutively active form of activin receptor-like kinase 6 (caALK6) and (**b**) runt-related transcription factor 2 (Runx2) after transfection by a quantitative polymerase chain reaction. Two, six and ten days after transfection, the mRNA expression of ALK6 and Runx2 was quantified. Data are means ± SDs, $n = 6$. caALK6, constitutively active form of activin receptor-like kinase 6; GFP, green fluorescence protein; Runx2, runt-related transcription factor 2.

Observation of GFP expression revealed that nanomicelles and FuGENE6 achieved similar levels of gene expression without showing any morphologic changes in the cells; this is evident in the phase contrast images (**Supplementary Figure S3**).

We then investigated the osteogenic differentiation after transfection of pDNAs expressing a constitutively active form of activin receptor-like kinase 6 (caALK6) and runt-related transcription factor 2 (Runx2), which have been shown to be a potent combination of genes for bone regeneration.[34] Osteogenic differentiation was evaluated by the expression of osteocalcin messenger RNA (mRNA), an osteoblast-differentiation marker. As shown in **Figure 3**, the time-dependent increase in osteocalcin expression was confirmed after transfection of caALK6 + Runx2 by both polyplex nanomicelles and FuGENE6. Using LPEI, in contrast, osteocalcin expression was at the same level as the control cells transfected with the GFP gene (data not shown). It is interesting that, on day 10, nanomicelles showed a more remarkable increase in osteocalcin expression than did FuGENE6, although both showed comparable gene expression without cytotoxicity by the luciferase and GFP reporter assays (**Figure 2a** and **b** and

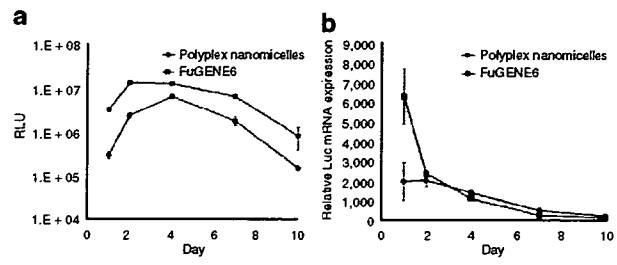

Figure 5 Evaluation of sustained expression of luciferase on mouse calvarial cells. (**a**) Luciferase expression measured by luminescence, which indicated the quantification of protein synthesis. Data are means ± SDs, $n = 12$. (**b**) Estimation of the corresponding messenger RNA (mRNA) expression by a quantitative polymerase chain reaction. For both, the mouse calvarial cells were transfected by luciferase-expressing plasmid DNA and the assays were done on days 1, 2, 4, 7, and 10. Data are means ± SDs, $n = 6$. RLU, relative light units.

Supplementary Figure S3). It is reasonable to assume that, with the same transfection procedure as used with the reporter genes, *caALK6* and *Runx2* were also expressed similarly by nanomicelles and FuGENE6. The reasons for this disparity in osteocalcin induction are unclear, but FuGENE6 may cause some appendant effect on cell differentiation that is difficult to detect by a nonspecific viability evaluation such as the MTT assay.[35] Regarding this concern we speculated that, since the difference was visible on day 10, the expression profile of the transfected genes might differ between nanomicelles and FuGENE6, thus affecting the outcome of the induction of cell differentiation.

To investigate this possibility, the time-dependent change of gene expression was quantified. As shown in **Figure 4**, the mRNA expressions of caALK6 and Runx2 showed similar profiles, where FuGENE6 initially induced expressions of ALK6 and Runx2 that were one order higher than nanomicelles, although the expressions sharply decreased with time. In contrast, the nanomicelles showed rather consistent gene expressions. For a detailed investigation, the luciferase gene was used and the protein systhesis and its mRNA expression were simultaneously quantified by a luminescence measurement and a quantitative polymerase chain reaction (PCR), respectively. As shown in **Figure 5**, FuGENE6 initially showed light emission (indicating the amount of synthesized protein) that was one order higher than did the nanomicelles. The highest expression was obtained on day 2. The initial mRNA expression was always high, but a rapid decrease was observed after day 2. In contrast, the polyplex nanomicelles showed fairly consistent gene expression profiles, giving the highest luciferase expression on day 4 and with sustained mRNA expression thereafter. Because cell differentiation would require some processes in signaling pathways inside the cells, it follows that such a continuous manner of gene expression by polyplex nanomicelles might contribute to the efficient induction of differentiation. Hence, the nanomicelle profile is a promising feature for *in vivo* bone regeneration.

In vitro transfection from gene-containing scaffolds

The *in vivo* gene transfer to a bone regeneration site should require the retention and gradual release of gene carriers. One promising approach is to incorporate the carriers into implantable scaffolds.

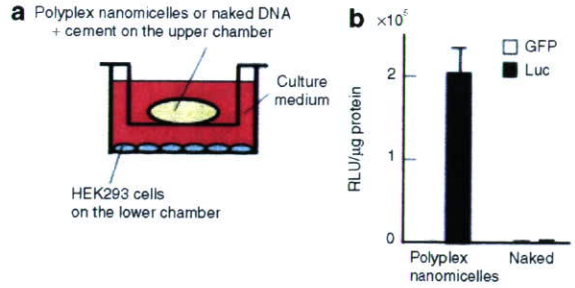

Figure 6 *In vitro* transfection by polyplex nanomicelles incorporated into calcium phosphate cement scaffold. **(a)** Schematic illustration of the *in vitro* transfection from the gene-containing scaffolds. The scaffold containing polyplex nanomicelles of PEG-b-P[Asp-(DET)] and plasmid DNA (pDNA) expressing luciferase gene or naked pDNA was plated onto the upper chamber of cell culture insert, and the HEK293 cells were plated onto the lower chamber. **(b)** Luciferase expression in HEK293 cells. After 5 days of transfection, luciferase expression was measured. The green fluorescence protein (GFP) gene was used as a negative control. Data are means ± SDs, $n = 3$. DET, diethylenetriamine; PEG, poly(ethyleneglycol); RLU, relative light units.

This form of gene delivery is called the gene-activated matrix, through which Bonadio *et al.* pioneered the incorporation of non-viral vectors in collagen scaffolds to stimulate bone formation in a rat defect model.[36] In this study, the polyplex nanomicelles were incorporated into a calcium phosphate cement scaffold by mixing. This process is highly biocompatible, bioactive (especially in bone tissue), moldable, and injectable.

In order to investigate whether or not the polyplex nanomicelles containing luciferase-expressing pDNA were delivered from the calcium phosphate cement scaffold, the scaffold was put into the culture medium of HEK293 cells for 5 days. The cement and the cells were physically separated by a filter to avoid direct contact between the cement and the cells, which could hinder the distinction between the release and the direct delivery of polyplex nanomicelles from the scaffold (**Figure 6**). As shown in **Figure 6b**, the cells cultured with the scaffold containing the polyplex nanomicelles exhibited apparent luciferase expression, whereas the cells cultured with the scaffold containing naked pDNA did not. Thus, the polyplex nanomicelles incorporated into the calcium phosphate cement scaffold successfully introduced the contained genes into the surrounding cells.

Next, to investigate how long the transfection by polyplex nanomicelles incorporated into the scaffold would last, the scaffold was placed on the culture dish and then mouse calvarial cells were plated on top of it and cultured for an extended period. Monitoring of luminescence using the IVIS Imaging System (Xenogen, Alameda, CA) revealed that the gene expression of mouse calvarial cells by the scaffold containing polyplex nanomicelles with luciferase-expressing pDNA increased, peaking near days 10 and 18, and then gradually declined to the background level approaching day 25 (**Supplementary Figure S4a**). Quantitative visualization of luminescence using this imaging system revealed that cells on top of the scaffold and in its close proximity were first transfected at days 2 and 10; subsequently, cells at some distance were transfected until day 25 (**Supplementary Figure S4b**). Thus, the polyplex nanomicelles incorporated into the scaffold delivered genes in a sustained manner.

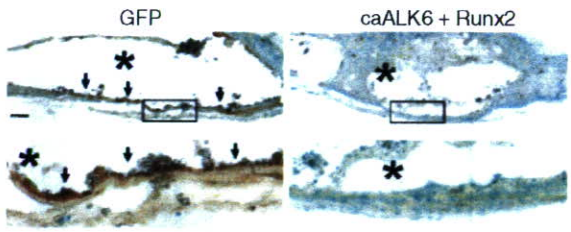

Figure 7 *In vivo* gene transfer by polyplex nanomicelles. Immunohistochemistry for green fluorescence protein (GFP) of calvarias implanted with the scaffold containing polyplex nanomicelles of PEG-b-P[Asp-(DET)] and plasmid DNA expressing GFP or caALK6 + Runx2 at 4 weeks after implantation. GFP protein was stained brown (arrows). The lower panel of each group shows a magnified view of the boxed area in the upper panel. Asterisks denote the remnants of calcium phosphate pastes. Scale bar: 200 μm. caALK6, constitutively active form of activin receptor-like kinase 6; DET, diethylenetriamine; PEG, poly(ethyleneglycol); Runx2, runt-related transcription factor 2.

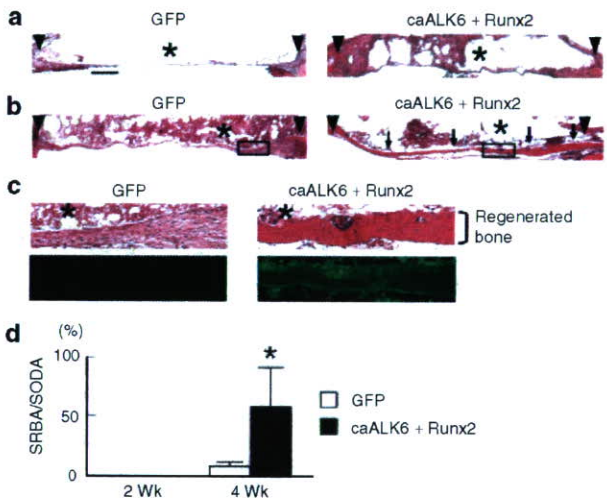

Figure 8 Bone regeneration by polyplex nanomicelles. **(a, b)** Histologic analyses of calvarias. The scaffold containing polyplex nanomicelles of PEG-b-P[Asp-(DET)] and plasmid DNA expressing green fluorescence protein (GFP) or caALK6 + Runx2 was implanted on the bone defect area on the mouse skull bone. At **(a)** 2 weeks and **(b)** 4 weeks after implantation, histologic and immunohistologic analyses were performed. Sections were stained with hematoxylin and eosin (H&E). Arrowheads denote defect edges; arrows, regenerated bones; asterisks, the remnants of calcium phosphate cement. Scale bar: 500 μm. **(c)** Magnified views of boxed areas in **b**. H&E (bright field views) and immunohistochemstry for type-I collagen (dark field views) were performed on serial sections. Green fluorescence indicates expression of type-I collagen. Asterisks, the remnants of calcium phosphate cement. **(d)** Quantification of bone regeneration. The ratio of the summation of the regenerated bone area to that of the original defect area (SRBA/SODA) in designated sections was histologically measured by NIH Image software. Data are means ± SD of five mice per group. $^*P < 0.01$ versus GFP at 4 weeks after implantation. caALK6, constitutively active form of activin receptor-like kinase 6; DET, diethylenetriamine; PEG, poly(ethyleneglycol); Runx2, runt-related transcription factor 2.

In vivo gene delivery to the bone defect area on the mouse calvarial bone

The data so far have shown that a localized and sustained system to deliver polyplex nanomicelles was successfully developed *in vitro* using the calcium phosphate cement scaffold. To

investigate whether or not this system is effective for *in vivo* gene delivery, the scaffold was molded to the fitting shape and implanted in mouse calvarial bone defects. After implantation of the scaffold containing polyplex nanomicelles with GFP pDNA, successfully transfected recipient cells were observed across a few layers from the implant surface by immunohistochemical analyses (**Figure 7**). The intensity of the staining was strongest in cells immediately adjacent to the scaffold, gradually declining with distance.

To investigate the therapeutic potential of this system, polyplex nanomicelles containing pDNAs expressing a caALK6 and Runx2, by which the osteogenic differentiation was induced on the calvarial cells *in vitro* (**Figure 3**), were incorporated into the calcium phosphate cement scaffold and implanted in the same model. At 2 weeks after implantation, no bone formation occurred in either the control group transfected with the GFP-expressing pDNA or the treatment group transfected with caALK6 + Runx2 expressing pDNA (**Figure 8a**). At 4 weeks after implantation, however, substantial bone formation covering the entire lower surface of the implant was induced only in the treatment group (**Figure 8b**), as confirmed by the quantitative analysis of the regenerated bone area (**Figure 8d**). The regenerated bone tissues exhibited a lamellar structure containing osteocyte-like cells and strongly expressed the type-I collagen protein (**Figure 8c**). On the other hand, the incorporation of neither the LPEI nor the FuGENE6 complex into the calcium phosphate cement scaffold generated any apparent bone formation at 4 weeks (data not shown). It should be noted that no sign of inflammation was observed in any group (**Figure 8a–c**). The results so far indicate that the polyplex nanomicelles incorporated into the calcium phosphate cement scaffold transfected the foreign genes to the cells in the vicinity of the scaffold, leading to a considerable increase in the rate of bone formation via the induction of osteogenic differentiation.

DISCUSSION

Many clinical fields demand useful non-viral gene delivery systems that satisfy high standards of both efficacy of gene introduction and low toxicity.[37] Bone tissue engineering would be a promising field; however, only a few trials have been reported so far. Bright *et al.* used a naked pDNA expressing OP-1 (BMP-7) gene, which was incorporated into a collagen scaffold, for a rat model of lumbar interbody arthrodesis.[38] Although bone formation was stimulated after 4 weeks, it was not as extensive as that observed after the injection of recombinant human OP-1 protein, in spite of considerably high dose of pDNA (250 μg/rat). Huang *et al.* combined poly(lactic-co-glycolic acid) scaffolds with 200 μg of condensed pDNA encoding BMP4 using branched PEI and implanted the scaffolds into rat cranial defects.[39] They successfully induced bone regeneration at the defect edges; however, osteoid and mineralized tissue was significantly increased after 15 weeks of implantation. The disparity between our results and theirs presumably resulted from the difference in the osteogenic signals. However, some toxic effects of PEI should also be taken into consideration: PEI was reported to be an apoptotic agent,[40] and indeed in our results it showed appreciable cytotoxicity (**Figures 1b** and **2b**) and an inability to induce differentiation. Directly comparing the capacity of their versus our method was not possible because Huang *et al.* did not provide data on the actual transfection efficiency; however, some negative effects of PEI on the cells in the vicinity of the scaffold may have caused the delayed induction of bone regeneration.

The considerably low dose of pDNA (1.3 μg/mouse) is also characteristic in our system. In previous studies of *in vivo* bone formation by non-viral gene delivery systems, a larger amount of pDNA (100 μg to 1 mg) was used.[38,39,41] We assume that this may be attributed to the capacity of polyplex nanomicelles to stably retain pDNA even in the scaffolds. Moreover, using the combination of osteogenic genes *caALK6* and *Runx2* contributed to the efficient osteoconductivity of our system. The cooperative action of this combination occurred through protein stabilization of core binding factor beta (Cbfb) and through induction of Runx2–Cbfb complex formation and its DNA binding, leading to the efficient induction of osteogenic differentiation.[34]

FuGENE6 has often been reported to have excellent transfection efficiency *in vitro*, including the induction of cell differentiation.[29–33] Indeed, in our results shown in **Figure 3**, comparable induction of osteocalcin expression was observed by both FuGENE6 and polyplex nanomicelles on day 5. It is interesting to note that, although the gene expressions evaluated by luciferase were consistently higher in FuGENE6 until day 10 (**Figure 5**), the osteocalcin induction was more remarkable in the nanomicelles on day 10 (**Figure 3**). The marked difference in gene expression profiles between nanomicelles and FuGENE6—especially when evaluated by mRNA expression—might influence the outcome of cell differentiation, which requires complex intracellular processes over an extended period. It is also possible that some toxicologic effects of the reagents might influence the cell reactivity, since many lipid-based transfection reagents were reported to induce changes in the expression of endogenous genes.[42] The study of toxicologic or pharmacologic effects of bioactive materials that might alter responses to delivered drugs or genes is now attracting attention as polymer (material) genomics.[43] From this standpoint, we have started comprehensive analyses of cell bioactivities after various transfection procedures, including the study of endogenous gene expression profiles using complementary DNA arrays. These results will be reported elsewhere in the near future.

The polyplex nanomicelles composed of PEG-b-P[Asp-(DET)] block copolymer and pDNA have demonstrated promising features for bone-regenerative gene therapy. The characteristics are summarized as: (i) good transfection efficiency with minimal cytotoxicity; (ii) sustained gene expression profile, which may be beneficial to cell differentiation; and (iii) excellent *in vivo* availability. Worth noting is that the enhancement of bone regeneration in this study was achieved without cell transplantation. Although the use of cell sources such as stem cells has been widely investigated, there remain many concerns for clinical application, such as the difficulty of finding an ideal cell source that meets both quality and quantity demands while also satisfying the concerns of medical costs and health risks.[44,45] Thus, it is desirable that cell transplantation be supplemented or replaced by innovations in other components of tissue engineering, signals, and scaffolds.